

UNDERSTANDING MIOCENE CLIMATIC WARMTH

A Thesis

Submitted to the Faculty

of

Purdue University

by

Ashley J. Dicks

In Partial Fulfillment of the

Requirements for the Degree

of

Master of Science

August 2019

Purdue University

West Lafayette, Indiana

**THE PURDUE UNIVERSITY GRADUATE SCHOOL**  
**STATEMENT OF THESIS APPROVAL**

Dr. Matthew Huber, Chair

Department of Earth, Atmospheric, and Planetary Science

Dr. Ernest Agee

Department of Earth, Atmospheric, and Planetary Science

Dr. Wen-Wen Tung

Department of Earth, Atmospheric, and Planetary Science

**Approved by:**

Dr. Daniel Cziczo

Department Head

## ACKNOWLEDGMENTS

Ashley J. Dicks thanks her committee and mentors:

I want to thank my advisor Professor Huber for being a wealth of knowledge - each time we talked I would learn something new from atmospheric science to an arbitrary topic. Also, thank you for providing an interesting research project. Thank you Professor Agee for being my number one fan throughout undergrad and graduate school and for helping me discover my love for research (and python). I would like to thank Professor Tung for bridging the gap between science and statistics and being a great teacher of everything in between the two. Professor Wu, thank you for getting me started in research as an undergraduate. Professor Chavas, thank you for helping me with becoming a better writer and for pushing me to excel in your classes. Dr. Muge Komurcu, thank you for your research on this project and providing help throughout the process.

Ashley J. Dicks thanks her colleagues, friends, and family:

I would not have survived graduate school without labmates, Dr. Paul Acosta and Dr. Jonathan Buzan. You both have provided me with research guidance and friendship, but also have taught me countless skills that I will be continuing to use throughout the rest of my career. Thank you Kalie Dicks for always being there as my best friend through all walks of life. Daniel Dicks, thanks for joining me at random coffee shops to work and bounce computer science questions/ ideas off of. Thank you Cole Griffin for your constant support, geeking out with me, and appreciating my puns (most of the time). Mom and Dad, you are both my role models in life - thank you for showing me how to work hard and stay sane, I love you.

Ashley J. Dicks thanks the following support:

The National Science Foundation (NSF) for providing the funding for this research project under NSF P2C2 1602905. Purdue University's Rosen Center for Advanced Computing for high performance computing resources used in the study.

## TABLE OF CONTENTS

	Page
LIST OF TABLES . . . . .	vii
LIST OF FIGURES . . . . .	viii
ABSTRACT . . . . .	xi
1 INTRODUCTION . . . . .	1
2 HYPOTHESIS . . . . .	5
3 BACKGROUND . . . . .	6
4 METHODS: DATA AND MODEL . . . . .	12
4.1 Data . . . . .	12
4.1.1 Pre-industrial Data . . . . .	12
4.1.2 Modern Data . . . . .	12
4.1.3 Miocene Data . . . . .	14
4.2 Model . . . . .	16
4.2.1 Fully Coupled Simulations . . . . .	17
4.2.2 Slab-Ocean Simulations . . . . .	18
5 EXPERIMENT DESIGN . . . . .	19
5.1 Pre-industrial Simulations . . . . .	19
5.2 Modern Simulations . . . . .	19
5.3 Miocene Simulations . . . . .	19
5.4 Control Cases . . . . .	20
5.5 Modified Cases . . . . .	20
6 RESULTS . . . . .	23
6.1 Surface Temperature . . . . .	23
6.1.1 Miocene . . . . .	28
6.2 Cloud Amount . . . . .	30
6.2.1 Miocene . . . . .	39
6.3 Fluxes . . . . .	44
6.3.1 Miocene . . . . .	52
6.4 Cloud Forcing . . . . .	55
6.4.1 Miocene . . . . .	60
7 DISCUSSION . . . . .	63
7.1 Temperature . . . . .	63

	Page
7.2 Cloud Amount . . . . .	64
7.3 Forcing and Fluxes . . . . .	65
8 CONCLUSION . . . . .	68
REFERENCES . . . . .	70

## LIST OF TABLES

Table	Page
5.1 Table of CESM 1.0.5 simulations ran with CAM5 used in this study. . . .	22
7.1 Table of values for the average shortwave cloud forcing (SWCF) and long-wave cloud forcing (LWCF) difference between modified cases and control cases. . . . .	67

## LIST OF FIGURES

Figure	Page
6.1 Surface temperature difference plot for the modified SLF simulations minus their respective control simulations are shown in the horizontal contour plots on the left. The zonal mean plot for SLF simulations (black) and their respective control simulations (red dashed) is shown on the right. . .	24
6.2 Time series plot of change in surface temperature for all slab-ocean cases years 0-100. . . . .	25
6.3 Represents the change in temperature averaged for the last 10 years plotted against the temperature averaged for the last 10 years of each modified simulation. . . . .	26
6.4 Vertical contour plots of temperature [K] for the modified SLF simulations and their respective control simulations. . . . .	27
6.5 Surface temperature difference plot for the modified SLF simulations are shown on the left. The zonal mean plot for SLF simulations (black) and reference simulations (red dashed) are on the right. . . . .	29
6.6 Vertical contour plots of temperature for the modified SLF simulations and their respective control simulations. . . . .	30
6.7 Total cloud amount difference plot for the modified SLF simulations minus their respective control simulations are shown in the horizontal contour plots on the left. The zonal mean plot for SLF simulations (black) and their respective control simulations (red dashed) is shown on the right. . .	31
6.8 High-level cloud amount difference plot for the modified SLF simulations minus their respective control simulations are shown in the horizontal contour plots on the left. The zonal mean plot for SLF simulations (black) and their respective control simulations (red dashed) is shown on the right.	33
6.9 Mid-level cloud amount difference plot for the modified SLF simulations minus their respective control simulations are shown in the horizontal contour plots on the left. The zonal mean plot for SLF simulations (black) and their respective control simulations (red dashed) is shown on the right.	35

Figure	Page
6.10 Low-level cloud amount difference plot for the modified SLF simulations minus their respective control simulations are shown in the horizontal contour plots on the left. The zonal mean plot for SLF simulations (black) and their respective control simulations (red dashed) is shown on the right.	37
6.11 Vertical contour plots of total cloud amount for the modified SLF simulations and their respective control simulations. . . . .	39
6.12 Total cloud amount difference plot for the modified SLF simulations are shown on the left. The zonal mean plot for SLF simulations (black) and reference simulations (red dashed) are on the right. . . . .	40
6.13 High-level cloud amount difference plot for the modified SLF simulations are shown on the left. The zonal mean plot for SLF simulations (black) and reference simulations (red dashed) are on the right. . . . .	41
6.14 Mid-level cloud amount difference plot for the modified SLF simulations are shown on the left. The zonal mean plot for SLF simulations (black) and reference simulations (red dashed) are on the right. . . . .	42
6.15 Low-level cloud amount difference plot for the modified SLF simulations are shown on the left. The zonal mean plot for SLF simulations (black) and reference simulations (red dashed) are on the right. . . . .	43
6.16 Vertical contour plots of total cloud amount for the modified SLF simulations and their respective control simulations. . . . .	44
6.17 Surface net shortwave flux difference plot for the modified SLF simulations minus their respective control simulations are shown in the horizontal contour plots on the left. The zonal mean plot for SLF simulations (black) and their respective control simulations (red dashed) is shown on the right.	45
6.18 Surface net longwave flux difference plot for the modified SLF simulations minus their respective control simulations are shown in the horizontal contour plots on the left. The zonal mean plot for SLF simulations (black) and their respective control simulations (red dashed) is shown on the right.	47
6.19 Top of model net shortwave flux difference plot for the modified SLF simulations minus their respective control simulations are shown in the horizontal contour plots on the left. The zonal mean plot for SLF simulations (black) and their respective control simulations (red dashed) is shown on the right. . . . .	49
6.20 Top of model net longwave flux difference plot for the modified SLF simulations minus their respective control simulations are shown in the horizontal contour plots on the left. The zonal mean plot for SLF simulations (black) and their respective control simulations (red dashed) is shown on the right.	51

Figure	Page
6.21 Surface net shortwave flux difference plot for the modified SLF simulations are shown on the left. The zonal mean plot for SLF simulations (black) and reference simulations (red dashed) are on the right. . . . .	52
6.22 Surface net longwave flux difference plot for the modified SLF simulations are shown on the left. The zonal mean plot for SLF simulations (black) and reference simulations (red dashed) are on the right. . . . .	53
6.23 Top of model net shortwave flux difference plot for the modified SLF simulations are shown on the left. The zonal mean plot for SLF simulations (black) and reference simulations (red dashed) are on the right. . . . .	54
6.24 Top of model net longwave flux difference plot for the modified SLF simulations are shown on the left. The zonal mean plot for SLF simulations (black) and reference simulations (red dashed) are on the right. . . . .	55
6.25 Longwave cloud forcing difference plot for the modified SLF simulations minus their respective control simulations are shown in the horizontal contour plots on the left. The zonal mean plot for SLF simulations (black) and their respective control simulations (red dashed) is shown on the right.	57
6.26 Shortwave cloud forcing difference plot for the modified SLF simulations minus their respective control simulations are shown in the horizontal contour plots on the left. The zonal mean plot for SLF simulations (black) and their respective control simulations (red dashed) is shown on the right.	59
6.27 Time series plots of shortwave cloud forcing and longwave cloud forcing across modified and control simulations. . . . .	60
6.28 Longwave cloud forcing difference plot for the modified SLF simulations are shown on the left. The zonal mean plot for SLF simulations (black) and reference simulations (red dashed) are on the right. . . . .	61
6.29 Shortwave cloud forcing difference plot for the modified SLF simulations are shown on the left. The zonal mean plot for SLF simulations (black) and reference simulations (red dashed) are on the right. . . . .	62
7.1 Cloud radiative forcing is represented in the $\tau$ (cloud optical depth) and Z (cloud top altitude) space. Contours are showing $W/m^2$ at the top of the atmosphere for daily averages. Figure is from Koren et al. 2010. . . . .	65
7.2 Trend lines of differences of the modified simulations by their control for top of model net longwave flux (FLNT), top of model net shortwave flux (FSNT), surface net longwave flux (FLNS), surface net shortwave flux (FSNS), longwave cloud forcing (LWCF), and shortwave cloud forcing (SWCF) plotted against the temperature for modified simulations (pre-industrial, modern 400 CO <sub>2</sub> , and modern 800 CO <sub>2</sub> ). . . . .	66

## ABSTRACT

Dicks, Ashley J. M.S., Purdue University, August 2019. Understanding Miocene Climatic Warmth. Major Professor: Matthew Huber Professor.

The mid-Miocene Climatic Optimum (MMCO), 17-14.50 million years ago, is studied using general circulation models (GCMs). This period of time is characterized by enhanced warming in the deep ocean and in the mid-to-high latitudes. Previous GCMs fail to accurately represent the warmer climate of the MMCO, providing evidence that other warming feedbacks are missing in the models. This study focuses on cloud feedbacks by modifying the Community Earth System Model (CESM 1.0) to explore the MMCO climate. We implement modifications in pre-industrial (284.7 ppm CO<sub>2</sub>) and modern slab ocean cases (367.0 ppm CO<sub>2</sub>, 400 ppm CO<sub>2</sub>, and 800 ppm CO<sub>2</sub>). One modified case showing the most potential implements an aerosol dependent ice nucleation mechanism and a theory based cloud phase separation. This modified case allows the model predicted aerosol concentrations to interact with the cloud microphysics and provide more realistic cloud water contents. The data shows an increase in surface temperature and increase in upper atmospheric cloud fraction when compared to the control case. Preliminary results suggest that this model is able to capture the mid-to-high latitude warming trends and weaker equator to pole temperature gradient.

## 1 INTRODUCTION

Paleoclimate modeling and data comparison plays an important role in exploring and understanding the function and processes of the climate system, allowing predictions to be made and tested against paleoenvironmental proxies [1]. These climate model simulations either succeed in matching proxy data or fail in doing so, providing opportunities to develop new physical understanding of conceptual models. Based on comparison with paleoclimate proxies, strengths and weaknesses can be analyzed for our current climate models, their components, and their sensitivity. Therefore, paleoclimate reconstructions are an important key to determining the response of different climate scenarios for our future because of their potential to be applied across time scales.

Many periods of time in Earth's history had sustained warming and are considered a greenhouse climate, lacking Arctic sea ice. Questions arise when looking at past greenhouse climates and address their key features of a) warmer global mean surface temperature, b) inner-continental reduced seasonality, and c) weaker equator to pole temperature gradient [1]. Not all past greenhouse climates though are the same and each contains different features. A period of time that serves interest to this research project occurs during the Miocene epoch which characterizes a long-term global cooling trend. During the early to mid Miocene climatic optimum (MMCO), occurring around 17-14.50 million years ago, Earth's temperatures were considerably warmer in the deep ocean and in the mid-to-high latitudes [2] [3] [4] [5] and global mean surface temperature was approximately 8°C warmer than modern [6]. More broadly, the middle Miocene (18-10 Ma), encompasses both the MMCO and the subsequent abrupt cooling and spread of the Antarctic ice-sheet, termed the middle Miocene climate transition (14.5-13.8 Ma) which appear to be associated with weak (50ppm) variations expansion in pCO<sub>2</sub> [7].

The MMCO has recently captured community attention because several proxy records indicate that atmospheric  $p\text{CO}_2$  was near present values [8] [9] [10], while a host of terrestrial paleoclimate and paleoenvironmental records [11] [12] [13] [14] [3] [15], and marine paleotemperature proxies [16] [17] [10] [18] demonstrate a level of pervasive global warmth unmatched since the Eocene.

In previous studies, the warmer extratropical temperatures were reconstructed in equilibrium with below-modern equatorial sea surface temperature records and 200-280 ppm  $\text{CO}_2$  [19] [20]. Recent studies have concluded that these cool tropical sea surface temperatures were incorrect and that the boron and alkenone  $\text{CO}_2$  reconstructions underestimated the actual  $\text{CO}_2$  concentrations. Kurschner et al. 2008 [21] used leaf stomatal studies to predict the MMCO  $\text{CO}_2$  concentrations to be in the range of 400-500 ppm. Also confirming the greenhouse gas concentration measurements, Foster et al. 2012 [9] used boron isotope-based reconstructions and Zhang et al. 2013 [10] used updated alkenone reconstructions. Thus, the MMCO has close to modern levels of  $\text{CO}_2$ , bringing about a bigger incentive to accurately reproduce the MMCO warming in our general circulation models (GCMs).

When using higher  $\text{CO}_2$  concentration, MMCO warming still has proven difficulty to reproduce using a moderate complexity Earth system model [22], slab-ocean and atmosphere model [23] [17], a fully coupled atmosphere-ocean model [24] [25], and using the improved Community Atmosphere Model version 4 (CAM4) framework with the Community Earth System Model (CESM1.0) [15]. These data suggest that existing greenhouse gas reconstructions and global warming hypotheses are insufficient to explain the extreme temperatures [15]. Therefore without increasing  $\text{CO}_2$  between the control and Miocene case, the global mean temperature increase of  $1.5^\circ\text{C}$  suggests that the temperature change could be explained by differences in topography, bathymetry, and vegetation [24].

As discussed above, the Miocene is characterized by conditions of global warmth and lessened meridional and zonal temperature gradients. Much of the tropical-to-subtropical warming in the Miocene is focused in ocean upwelling zones, producing

anomalies of about 3 to 9 °C increase relative to today [26] [27] [28] [29]. These results suggest novel ocean-atmosphere interactions in a warmer world. Yet, doubts have been raised regarding the interpretation of these proxy records [30] [31] [32] [33] [34] [35] [36] [37] [18]. Recent work OBrien et al., 2014 [18] using TEX86 suggests higher temperatures in the Pacific and Atlantic Warm Pools than previously inferred. Among the traditional mechanisms proposed to explain weakened temperature gradients, warming preferentially in the upwelling zones, and deep tropical thermoclines are: enhanced high latitude fresh water forcing [38] [39], opening of the Central American/ Panamanian seaway [40] [41] [42], and the rearrangement of the islands in the maritime continent [43] [44]. These processes are represented, albeit imperfectly, in the latest generation of climate models, yet while much progress has been made in modeling (for example by the PlioMIP effort), substantially weakened gradients are not reproduced in the Miocene simulations [24] [45] [15]. Fedorov et al. (2013) [46] examined many of these mechanisms in a single modeling framework and concluded that none seems to be able to explain the observed patterns on its own. At higher latitudes, the data more clearly converge on a warming that is impossible to explain with existing models. In other words, the signal to noise ratio is better. Proxy evidence suggests that the mid-Miocene Arctic, was about 11-19°C warmer than at present [3] [24] [45] [15] [47].

Goldner et al. 2014 [15] also explored non-CO<sub>2</sub> forcings that could have played a role in the MMCO pronounced warmth, with the conclusion that an explanation of the warmth will involve an understanding nonlinear feedbacks to the imposed variations [48] [5] [49]. Thus while past climates like the Miocene are clearly not a perfect direct analogue of near-future warming [50] [51], understanding its climate can be most useful in exposing feedbacks that may be active in a future warming as well.

One of the largest uncertainty in the general circulation models (GCMs) is the problem of cloud representation and cloud feedbacks as they continue to be the greatest cause of ambiguity for estimates of Earth's climate sensitivity from GCMs [52].

Clouds affect GCMs by their radiative properties and precipitation properties. Clouds can reflect sunlight and can trap Earth's outgoing thermal radiation giving them the ability to either have a net cooling effect or a net warming effect, respectively. The scattering of sunlight from aerosols generates a net cooling at Earth's surface and the absorption of aerosols causes warming, influence atmospheric stability, and decrease cloud formation [53]. In GCMs this effect is hard to parameterize. This source of uncertainty is partly due to the fact that cloud processes in our atmosphere occur at the microscopic scale, consequently they cannot be explicitly represented in GCMs and have to be parameterized [54]. GCMs produce errors when tuning parameters, such as the processes listed above, are unphysical [55] [56]. Mixed phase clouds are a combination of liquid water droplets and ice crystals, which can coexist in our atmosphere. This coexistence brings uncertainty in the cloud radiative and thermodynamic properties [57]. Therefore, simulating cloud phase correctly is a prevailing problem in cloud physics research [57] [58].

For years, clouds were treated simply in models with a temperature separation of cloud phase such as in NCAR's CAM 4.0 and other older versions of the atmospheric model component. In new generations, aerosols and aerosol-cloud interactions, nucleation and growth of ice crystals are included in the GCMs and is implemented in CAM 5.0 (CAM5). These advancements haven't yet been fully implemented to simulations of paleoclimates. Cloud radiative feedbacks could explain some of the warming observed in the MMCO, which previously could not be explained alone by higher CO<sub>2</sub> concentration simulations.

## 2 HYPOTHESIS

The goal of this study is to test hypotheses that cloud microphysical property-aerosol feedbacks explain Miocene warmth at near-modern greenhouse gas concentrations of approximately 400 ppm. Two important cloud properties examined in this study are those of ice nucleation and mixed phase clouds. Changes are made to provide more realistic modeling and representation of these properties and their response in the climate system. Both ice nucleation and mixed phase clouds directly affect the cloud radiative properties and also affect other feedbacks in atmospheric models. In order to explore the hypotheses of how clouds may have maintained a warm climate in the Miocene, first the atmospheric model of CAM4 was compared to CAM5 with improved microphysics, and then the atmospheric model (CAM5) was adapted in new cases where cloud parameterization and schemes were explored.

*Please note, that because paleoclimate models take a long time to run out to equilibrium, pre-industrial and modern day simulations with varying  $CO_2$  are first tested against the hypothesis. Fully-coupled Miocene simulations are also tested and preliminary results can be drawn from those simulation outcomes.*

### 3 BACKGROUND

Atmospheric climate models are continuing to grow and develop with the advances in technology and computing, allowing scientists to further explore the addition of atmospheric dynamics, physics, and parameterization schemes into working GCMs. The hypothesis is that climate models are missing key cloud processes or feedbacks that may have kept Miocene climate warm at relatively low  $\text{CO}_2$ . Specifically it focuses on the microphysics schemes included in the Community Atmospheric Model and the development of a more accurate representation of these properties, starting from the advancements made from CAM4 to CAM5 and making further enhancements to CAM5.

CAM4 is an atmospheric general circulation model built and designed by the National Center for Atmospheric Research (NCAR) with collaboration from the Atmospheric Model Working Group. CAM4 represents the atmosphere vertically with a 26 level hybrid sigma-pressure coordinate system and defaults to the finite volume scheme for the dynamical core component. The main components represented in CAM4 are (moist) precipitation, cloud, radiation, surface atmospheric properties, and turbulent mixing. These four main atmospheric factors also consist of sub-components. This is the sixth version of the atmospheric model and provides enhancements on CAM 3.0 the previous model [59].

Such enhancements on the current Zhang and McFarlane 1995 [60] deep convection parameterization include the Convective Available Potential Energy (CAPE) calculations, sub-grid scale Convective Momentum Transports (CMT) modifications from Richter and Rasch 2008 [61], and an adjusted dilute plume computation by Raymond and Blyth 1986, 1992 [62] [63]. These modifications show significant improvements of the modified El Nino [59], and in the Hadley circulation and tropical convection [61]. Along with the modifications to deep-convection, cloud fraction has

also been modified in polar climates following Vavrus and Waliser's (2008) [64] calculation of stratiform cloud, reducing the warm bias produced by earlier versions of the model.

Model flexibility is increased in the newer model as well as within the climate system model as a whole, in part thanks to the new parameterization of non-convective cloud processes allowing precipitate to be a mixture of rain and snow. There are two components for the new parameterization: a macroscale component [65] and a bulk microphysical component [66]. Included in the new model is the treatment of aerosols, which replaces the uniform background boundary-layer aerosol. There are five aerosols described in the model: sea salt, soil dust, black and organic carbonaceous aerosols, sulfate, and volcanic sulfuric acid. When it comes to representing clouds, CAM4 discerns between cloud drop effective radius over the land and ocean, and over pure surfaces of sea ice and snow cover. When over landmasses, temperature drives the cloud drop effective radius. Vertical cloud overlap parameterization follows Collins 2001 [67] and clouds are all treated as gray bodies. Their emissivity is dependent on “cloud phase, condensed water path, and effective radius of ice particles” [59]. Overall, CAM4 incorporates improvements to the physics package providing a significantly improved atmospheric model [59].

CAM5 includes enhancements to the physical packages on the previous atmospheric model component from NCAR, CAM4 described above, such that the transition between the standalone and the fully coupled experiment framework is much stronger [68]. Modifications to CAM5 include, a new moist turbulence scheme, a new shallow water convective scheme, updated stratiform microphysical processes, a revised cloud macrophysics scheme, and a 3-mode modal aerosol scheme (MAM3). The combination of these improvements in physical parameterization allow for the simulation of complete aerosol cloud interactions of “cloud droplet activation by aerosols, precipitation processes due to particle size dependent behavior, and explicit radiative interaction of cloud particles” according to the Description of the NCAR Community

Atmosphere Model (CAM 5.0). [68] A huge development to the atmospheric model is that CAM5 has the ability to model cloud-aerosol indirect radiative effects.

The new moist turbulence scheme allows for the simulation of full aerosol indirect effects within stratus. The model now clearly simulates stratus-radiation-turbulence interactions based on a diagnostic Turbulent Kinetic Energy (TKE) formulation and a first order K-diffusion scheme with entrainment from Bretherton and Park 2009 [69].

The new shallow convective scheme is designed to prevent double counting by communicating with the moist turbulence scheme, an issue associated with previous versions of the model. Based on Parks and Bretherton 2009 [69], the scheme simulates the spatial dispersion of shallow convective activity by using a more accurate plume dilution equation and closure. Assuming little fractional area and steady state convective updrafts, the updraft vertical momentum equation is used to estimate the vertical velocity and fraction of the convective updraft.

Stratiform microphysical processes follow parameterization by Morrison and Gettelman 2008 [70], utilizing two-moment formulation of cloud ice and droplets. The liquid and ice particles evolve based on grid-scale advection, convective detrainment, turbulent diffusion and other microphysical properties. Aerosol chemistry, temperature, and vertical velocity determine the activation of cloud droplets, TKE approximations determine sub-grid scale vertical velocity, and many mechanisms determine ice crystal nucleation [71], as well as modifications to allow ice supersaturation [72].

The macrophysics cloud scheme is revised to allow for cloud fraction to be consistent with cloud condensate [73]. Liquid cloud fractions are triangularly distributed based on total relative humidity and ice cloud fraction is obtained from a modified relative humidity over ice, including the amount of ice condensate [72]. These two fractions are treated as separate calculations.

Another huge advancement in CAM5 is the new 3-mode modal aerosol scheme (MAM3) [74]. This scheme allows for mixed representation of concentration numbers and masses of accumulation and coarse aerosol modes, offering a blended version of the more involved 7-mode scheme. The Lamarque et al. 2010 IPCC AR5 emission

dataset [75] provides the definition of anthropogenic emissions (industrial, native, and agricultural). Bond et al. 2007 [76] and Junker and Liousse 2008 [77] provide emissions of black and organic carbon, and sulfur dioxide emissions come from Smith et al. 2001, 2004 [78] [79]. For natural emission sources the AEROCOM emission datasets are used.

The calculations and specifications for aerosols, liquid cloud droplets, hydrometeors, and ice crystals are used as input for the radiation scheme. These calculations are from the microphysics and aerosol parameterization quantities. Based on MAM3, the aerosol optical properties are defined [80] and combined before the radiative calculation. The liquid cloud optical properties follow Wiscombe 1996 [81] calculations and ice-cloud optics follow Mitchell 2002 [82]. Again, these properties are combined before the radiative computations. The updated radiative scheme (Rapid Radiative Transfer Method for GCMs, RRTMG) follows Iacono et al. 2008 [83] and Mlawer et al. 1997 [84] to apply a correlated-k method for computing radiative fluxes and warming rates. The RRTM separates into 14 short-wave bands (0.2  $\mu\text{m}$  to 12.2  $\mu\text{m}$ ) and solar irradiance is specified based on the Lean dataset [85]. The RRTM also separates into 16 long-wave bands (3.1  $\mu\text{m}$  to 1000  $\mu\text{m}$ ). The new RRTMG contains modifications to the RRTM, such as implementing the Monte-Carlo Independent Column Approximations [86] for sub-grid scale cloud variability, to “retain superior offline agreement” compared to older versions of CAM radiation packages.

As the Community Atmospheric Model advances, it is still missing some key processes that could affect the model's output. These processes explored in this study deal with mixed phase clouds and ice nucleation.

Mixed phase clouds in our atmosphere directly effect the cloud radiative and thermodynamic properties of the cloud [57]. Mixed phase clouds can also effect the climate model from amplifying and/or dampening other feedbacks represented in the model producing a wide range of climate responses.

Komurcu et al. 2014 [57] and Cesana et al. 2015 [87] found that GCMs underestimate the supercooled liquid fraction in mixed phase clouds. CAM5 does not

accurately simulate the fraction of supercooled liquid, liquid droplets, and ice crystals [54] and tuning the model alone will not solve this issue. Therefore, uncertainties in climate sensitivity and response can be reduced by better representation of cloud phase in comparison to observations and further understanding the microphysical processes associated with mixed phase clouds [54]. Another process identified as important to the climate model accuracy and uncertainty is with the ice nucleation mechanism.

Ice nucleation is the process of ice formation and it influences the radiative properties of the climate system. Ice nucleation depends on other favorable atmospheric properties of relative humidity, cloud temperature, and a nucleation surface [88]. Different aerosols present at a given moment impact the properties of ice nucleation. It is not well understood and looks to schemes and parameterization to capture. Strides to further understand and develop schemes have come from laboratory data, field data, and a combination of the two. Recently, a study conducted by DeMott et al. 2015 [89], worked to integrate laboratory and field data to develop empirical parameterization. Their work used measurements from the continuous flow diffusion chamber (CFDC) at Colorado State University, following DeMott et al. 2010 findings that predicted ice nucleation particle concentrations incorporated with aerosol number concentrations greater than  $0.5 \mu\text{m}$  allowed for improvement in the predicted ice nucleation particles instead of just incorporating temperature alone [90]. Further, DeMott et al. 2015 suggests that an acceptable first-order approximation for climate models is to consider all mineral dust as one category of ice nucleating particle [89]. This approximation has applications in models based on variables to predict the ice nucleation particle concentrations [88] and has been successfully applied in regional model simulations [91].

Research has progressed, as discussed in the sections above, to further enhance atmospheric climate models such as CAM. It is clear that as understanding of the microphysical properties of aerosol and clouds advance, so should the schemes representing them. Implementation of the concepts into models can create a more accurate

representation of climate. In this study, the atmospheric model is modified for three unique cases in order to explore the effect of cloud microphysical property-aerosol feedbacks on the MMCO warming.

## 4 METHODS: DATA AND MODEL

### 4.1 Data

In this section we summarize pre-industrial, modern, and paleoclimate data as well as CALIOP observations that are utilized in this study. A break down of proxy data and conditions will provide an overall picture of the different times analyzed in this study.

#### 4.1.1 Pre-industrial Data

Pre-industrial data is used from the year 1850 and is from CESM's pre-industrial component set.

#### Boundary Conditions

The pre-industrial data uses near modern topography.  $\text{CO}_2$  is set to 284.7 ppm to follow the preset value for pre-industrial component sets of the model used. Other greenhouse gas concentrations are prescribed at typical pre-industrial values. The solar insolation is set to  $340.0 \text{ w/m}^2$ . MAM3 aerosols from 1850 emissions are prescribed in the atmospheric component of the model, which contains three aerosol modes of aiten, accumulation, and coarse [92]. Orbital parameters follow the pre-industrial configuration.

#### 4.1.2 Modern Data

The modern data sets come from the CESM component sets available for the year 2000 and on.

## Boundary Conditions

The control value of CO<sub>2</sub> is set to 367.0 ppm and modern topography is followed in the modern cases. Solar insolation is prescribed to 341.6 W/m<sup>2</sup>. Greenhouse gas amounts are also prescribed to modern day values at the year 2000. Orbital parameters follow present day configuration.

## CALIOP Observations

The Cloud-Aerosol Lidar with Orthogonal Polarization (CALIOP) is a lidar carried on the sun-synchronous polar orbit of the Cloud-Aerosol Lidar and Infrared Pathfinder Satellite Observations (CALIPSO) and has a 16 day repeat cycle [53]. CALIOP views two-wavelengths (532 nm, 1064 nm) at near-nadir and contains a polarization-sensitive lidar (532-nm beam polarized) providing the scientific community with new observational based atmospheric measurements producing a footprint across Earth of 70m. Using the lidar technology, high resolution profiles of aerosols during day and night time as well as over highly reflective surfaces such as sand and snow can be accessed. Lidar is able to pass through high thin clouds and CALIOP gives a vertically resolved measurement of ice-water phase through depolarization measurements by lidar backscatter signal, generating a profile for a broad portion of the atmosphere [53]. The lidar has a resolution of 60 m in the vertical and 335 m in the horizontal below 8.2 km in altitude and 60 m in the vertical and 1 km in the horizontal above 8.2 km [54]. It is designed to contain the full range of backscatter from molecular, aerosol, and cloud within 5 orders of magnitude. Having a data turnaround time of about 5 days, CALIOP gives a complete dataset for global aerosol model validation.

An important part in this study is CALIOPs ability to identify cloud ice-water phase using a discrimination algorithm [53]. The lidar transmits a polarized pulse that will be returned in perpendicular and parallel backscatter. This ratio returned as the volume depolarization value determines whether the transmission is scattered by

ice or by liquid droplets [93] as well as using temperature and height of the layer [94] to identify cloud ice-water phase. CALIOP also provides discrimination between cloud and aerosols using its cloud-aerosol discrimination (CAD) algorithm. The CAD algorithm is based on statistical properties derived from CALIOP observations of layer volume ratio color, mean attenuate back scatter coefficient, location and latitude, depolarization, and the center of the layer height [54]. Aerosol types that can be identified from CALIOP includes various dust types, smoke, and clean or polluted continental, and clean marine [95].

### 4.1.3 Miocene Data

Based on paleoclimate proxies, data (i.e.: temperature and CO<sub>2</sub> concentration) can be derived and implemented during the MMCO event [6]. Both terrestrial and marine proxy data have indicated the MMCO's globally warmer climate conditions [4] [5] [96] [97] [14] [98]. Such that the marine proxy data reveal deep ocean temperatures and mid to high latitude ocean temperatures are warmer based on deep-sea benthic foraminiferal oxygen-isotopes [4] [5] as well as sea surface temperatures (SSTs) being re-evaluated as higher than modern temperatures [17] [99]. The terrestrial, paleobotanical, records also indicate the humid environment found in the MMCO, lower seasonality, a weak equator-to-pole temperature gradient, and higher temperatures over the continents [97] [98] [14].

### Boundary Conditions

All of the model simulations are done following the topography and bathymetry described in Herold et. al 2011 [24]. Orbital parameters follow the pre-industrial configuration such as in the pre-industrial simulations. This section provides an explanation of the implemented changes to the Miocene dataset.

The main modifications from the modern topography to the Miocene topography are to the areas of the Tibetan Plateau, Andean Cordillera, North and South America,

the ice-sheets and the northern European continental shelf [100]. Since the Miocene, the plate tectonic and topographic changes have been relatively small, allowing broad adjustments to the topography to be satisfactory in representing this period. Another benefit is the ability for this method to continue to contain roughness in the dataset which can be lost when topographic data sets are created from the ground up. The following is brief summary of topographic changes to the Miocene dataset.

Herold et al. 2012 [45] found that with the Greenland-Scotland Ridge absent and Iceland below sea level, deep water formation was altered. Therefore, in the updated dataset, the Greenland-Scotland Ridge is implemented as shallow (-100 m) with a deep Faroe-Shetland Channel (approximately -4,500 m) and Iceland is implemented as sub-areal based on fossil flora depth estimates from deep sea drilling records. These drillings show the Madagascar Ridge at 900 m, the Mascarene Ridge at 700 m and the Kerguelen Plateau at 2000 m depth. These ridges are adjusted to their respective depths following Herold et al. 2011 [24]. In South America, the Amazon River is removed based on evidence suggesting the early Miocene Amazon drained into the Caribbean and then the middle to late Miocene Amazon drained towards the Atlantic [101] [102] [103]. For these reasons, a wetland plant functional type is used during vegetation input when representing the Amazon. Moving north, a deep meridional channel is represented between the Pacific and Atlantic Oceans following Iturralde-Vincent 2006 [104] for the Panama gateway.

From the Eocene-Oligocene Transition (approximately 34 Ma) and Middle Miocene Climate Transition (approximately 14 Ma), the Cenozoic history of the Antarctic ice-sheet is consistent in showing significant fluctuations in volume and extent. Although, the West Antarctic Ice Sheet is found to be very small to non-existent small [105] [106] [107]. Based on the extreme warmth in the Miocene, implementation of an ice-volume and sea-level rise are consistent with the warmer temperature and obtained from a combination of two datasets. Ice sheet model output provided by David Pollard, from the methodology in Pollard and DeConto 2009 [108], has been used as a base for the Antarctic topography and ice-sheet mask. This ice-sheet con-

sists of 6.5 million km<sup>3</sup> of ice overlaying a modern bedrock, with a majority of the ice located in the East Antarctica. When looking at West Antarctica, the topography is modified using an ANTSCAPE dataset (contains 40 percent maximum Eocene topography with 60 percent modern bedrock) based on findings from Wilson and Luyendyk 2009 [109] that suggests the West Antarctic bedrock was higher than modern in the Eocene-Oligocene. Therefore, the ice-sheet should be between the Eocene high value and the modern value for the Miocene. The Greenland ice-sheet is simulated using ice-sheet distributions from Aisling Dolan's Pliocene ice-sheet modelling intercomparison project. For this project, the ice-sheet was represented under 560 ppm CO<sub>2</sub> with mean Pliocene orbit parameters, providing an acceptable representation for the MMCO based on only small changes to the orbital parameters between these time periods and gives a volume of approximately 0.294 million km<sup>3</sup>. This brings about a total global ice volume of approximately 6.8 million km<sup>3</sup> versus the modern volume of 29.6 million km<sup>3</sup> [110] [111]. Based on this value, the sea-level is set to 50 m above the present [100] to follow the modern sea-level to sea-ice volume relationship.

These updated Miocene topography and bathymetry datasets are used for all of the Miocene CESM cases described in this study.

## 4.2 Model

The Community Earth System Model (CESM) is developed by the National Center for Atmospheric Research as a community global climate model. CESM runs fully coupled simulations with atmosphere, ocean, land, and sea-ice geophysical model components and uses one central coupler to link each component. The coupler reads information from each component and then calculates and transmits the information back to each individual component as needed [112]. This process occurs as the model integrates over time.

### 4.2.1 Fully Coupled Simulations

The CESM components used in this study is CAM5 for modeling the atmosphere, Parallel Ocean Program (POP2) for modeling the ocean, CLM4 for modeling the land, and CICE for modeling the sea ice. CAM5 was described in Chapter 2 "Background". The POP2 is the ocean general circulation model that solves three-dimensional primitive equations at level coordinates and is the ocean component that CESM runs [113]. POP2 is a level-coordinate ocean general circulation model that continues to advance through updated physics packages and features provided by various scientists around the world [113]. This model describes ocean dynamics by solving the three-dimensional primitive equations and by treating the ocean as a thin stratified fluid. Using hydrostatic and Boussinesq approximations with the momentum, continuity, and hydrostatic equations, as well as with the equation of state and tracer transport equations, the ocean can be represented in general coordinates. The version of POP2 implemented in this study contains 60 vertical levels at a resolution of 1 degree. Fully coupled CESM utilizes the Community Land Model (CLM) which represents the land surface features related to land biogeophysics, humans, ecosystem dynamics, the hydrological cycle, and biogeochemistry as well as others not listed [114]. CLM4, the version used in this study, can calculate up to 15 possible plant functional types [115]. The Community Ice Code (CICE) is the sea-ice component that CESM runs and is the latest version of the Los Alamos Sea Ice Model released. CICE has interacting components of a thermodynamic model, an ice dynamic model, a transport model, and a ridging parameterization [116].

Fully coupled CESM simulations involve running all components of the model linked together using the coupler. These simulations include atmospheric, land, sea-ice, and ocean components that are described above.

### 4.2.2 Slab-Ocean Simulations

Slab-ocean simulations used in CESM is a simplified ocean model ran with the full atmospheric component of the model, CAM described in Chapter 3. Instead of using POP2 like in the fully coupled simulation, DOCN is the model used for the ocean component [112]. The temperature of the slab-ocean is simply calculated using depth and surface energy fluxes. The ocean heat transport, Q-flux, is improved to be based off of fully coupled simulations and not observations and now it uses mixed-layer depth, mixed-layer temperature, and surface net energy balance to calculate [117]. The model is an approximation of a well-mixed ocean and is ran across all ocean grid points in the simulations [118]. The components of CAM, CLM, and CICE are also active in this version of the model, described in previous sections.

## 5 EXPERIMENT DESIGN

CESM 1.0.5 simulations are performed with the implemented modifications to CAM5 using initial and boundary conditions described in Section 4.1 "Data".

### 5.1 Pre-industrial Simulations

The pre-industrial simulations ran in this study are ran as slab-ocean models. A full functioning atmospheric model, CAM5, is ran coupled to the DOCN slab-ocean with the other components of CLM and CICE. The slab-ocean simplifies the simulations and is used in this study since modifications are only made to the atmospheric component of CESM. The model has  $1.9^\circ \times 2.5^\circ$  horizontal resolution with 30 vertical levels in the atmospheric component. The ocean component has  $1^\circ$  resolution each pre-industrial simulation is ran for 100 years.

### 5.2 Modern Simulations

Like the pre-industrial simulations, slab-ocean configurations for CESM are also used in the modern day simulations. CAM5, CLM, CICE, and DOCN are coupled together and ran for 100 years for all of the modern day simulations. These cases follow the boundary conditions, topography, and orbital parameters outlined in the previous section.

### 5.3 Miocene Simulations

The CAM5 simulations are run using Miocene boundary conditions at  $1.9^\circ \times 2.5^\circ$  horizontal resolution with 30 vertical levels. These cases are fully coupled to the other components of CESM1.0.5 land, ocean, and sea ice. Vegetation cover follows

that of Herold et al. 2010 [119] with no ice cover over Greenland and reduced ice cover over Antarctica [106]. Topography is described in Herold et al. 2011 [24]. Orbital parameters follow the pre-industrial configuration, discussed in the "Data" section.

*Note: these simulations are still running, but preliminary results will be provided in this study.*

#### 5.4 Control Cases

Control cases are set up for pre-industrial, modern, and Miocene simulations. Pre-industrial and modern control simulations do not have any changes to the CESM component set definitions used and are run as slab-ocean models. Values of 284.7, 367.0, 400.0, and 800.0 ppm for the CO<sub>2</sub> in the pre-industrial and three modern control cases are implemented, respectively. The control case for the fully-coupled Miocene simulations is run as described above without any modifications made to CAM5. The CO<sub>2</sub> concentrations for the Miocene control case are set to near modern values at 400 ppm as well as a more extreme value of 800 ppm.

#### 5.5 Modified Cases

A total of four different cases are set up and modified for pre-industrial and modern slab-ocean models. Two fully coupled simulations are created for the Miocene to include modifications to their atmospheric component as described below. These Miocene cases are run at 400 and 800 ppm CO<sub>2</sub> in order to test climate sensitivity and to be compared with the 400 and 800 ppm CO<sub>2</sub> modern simulations. CESM 1.0.5 is used with CAM5 for the atmospheric component as the base for the modified (SLF) simulations and the following adjustments to the atmospheric model are described below.

An aerosol dependent ice nucleation mechanism [89] is implemented to replace the default temperature and supersaturation based ice nucleation parameterization [120] in CAM5. This ice nucleation scheme diagnoses concentrations of ice nuclei based

on field observations from various seasons and regions. By using these prognostically calculated aerosol concentrations a more realistic number for ice nucleating particle concentrations is determined [54]. With this, the 3-mode aerosol scheme of CAM5, Module Aerosol Mode 3, is used. The implemented parameterization from DeMott et al. 2015 [89] allows the model-predicted aerosol concentrations to interact with the cloud microphysics and provide more realistic cloud water contents, and in turn cloud radiative feedbacks.

A theory-based cloud phase separation [121] is also implemented in CAM5 instead of observation-based phase separation algorithms. The reason this algorithm is applied rather than an observation-based phase separation algorithm like Tan and Storelvmo 2016 [54] is twofold. First, the observation-based phase separation algorithm is based on CALIOP retrievals, which are very high-resolution but have limited record. Data from CALIOP are available since 2008 and due to a change in instrument angle and calibration, the available number of observations that can be utilized are limited. Second, the aerosol types and abundances in paleoclimates are different. Hence, though not studied in detail, aerosol-cloud-cloud phase interactions may be different now than in the past, which would affect cloud radiative feedbacks and the degree of warming at the surface.

Table 5.1.: Table of CESM 1.0.5 simulations ran with CAM5 used in this study.

CESM 1.0 Simulations				
Name	Model Type	Time	Modifications	CO <sub>2</sub>
PI Control	Slab Ocean	1850	None	284.7 ppm
PI Modified	Slab Ocean	1850	SLF	284.7 ppm
Modern Control	Slab Ocean	2000	None	367.0 ppm
Modern Modified	Slab Ocean	2000	SLF	367.0 ppm
400 CO <sub>2</sub> Control	Slab Ocean	2000	None	400.0 ppm
400 CO <sub>2</sub> Modified	Slab Ocean	2000	SLF	400.0 ppm
800 CO <sub>2</sub> Control	Slab Ocean	2000	None	800.0 ppm
800 CO <sub>2</sub> Modified	Slab Ocean	2000	SLF	800.0 ppm
MIO 400 CO <sub>2</sub> Control	Fully Coupled	Miocene	None	400.0 ppm
MIO 400 CO <sub>2</sub> Modified	Fully Coupled	Miocene	SLF	400.0 ppm
MIO 800 CO <sub>2</sub> Control	Fully Coupled	Miocene	None	800.0 ppm
MIO 800 CO <sub>2</sub> Modified	Fully Coupled	Miocene	SLF	800.0 ppm

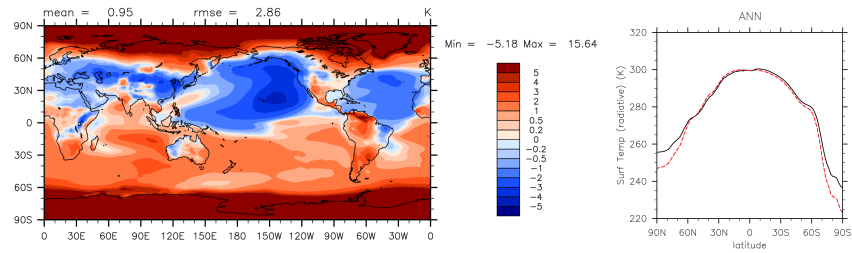
## 6 RESULTS

### 6.1 Surface Temperature

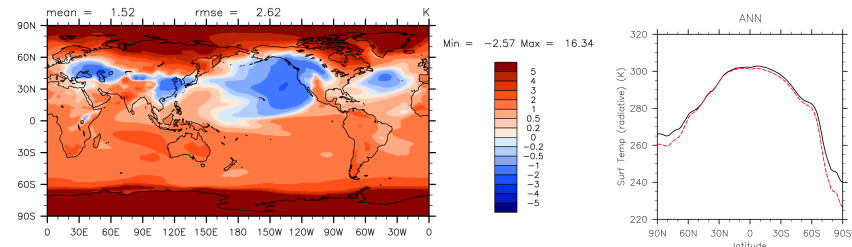
The annual difference in surface temperature for the control case and the modified case for each slab-ocean simulations of pre-industrial, modern, modern at 400 CO<sub>2</sub>, and modern at 800 CO<sub>2</sub> are compared (Figure 6.1 and Figure 6.2). Next to the surface maps are the zonal mean plots for surface temperature in Figure 6.1. When CO<sub>2</sub> is increased (moving down the figure) there is a noticeable increase in surface temperature, with Plot D showing the modern 800 simulation having surface temperature increase across the entire globe. Mean temperature values go from 0.95 increase in the PI simulation to 2.83 in the modern 800 simulation. The areas that are increasing in temperature the most are the polar regions. All of the zonal mean plots show the largest separation from the red control line and the black modified case line at the high latitudes to about 60°N and 60°S. Each of the zonal mean plots follow the same shape and show the polar region temperature increase with the degree of warming increasing with increasing CO<sub>2</sub>.

## Surface Temperature Difference: Modified - Control

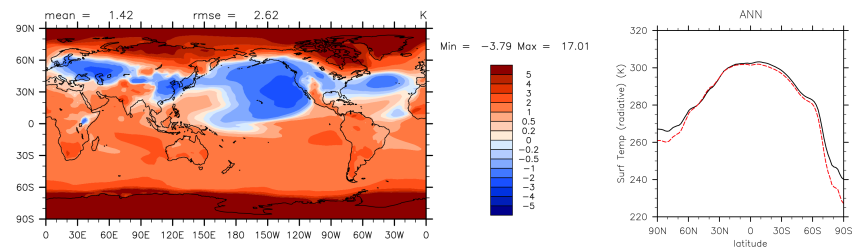
(a) PI simulation



(b) Modern simulation



(c) Modern 400 simulation



(d) Modern 800 simulation

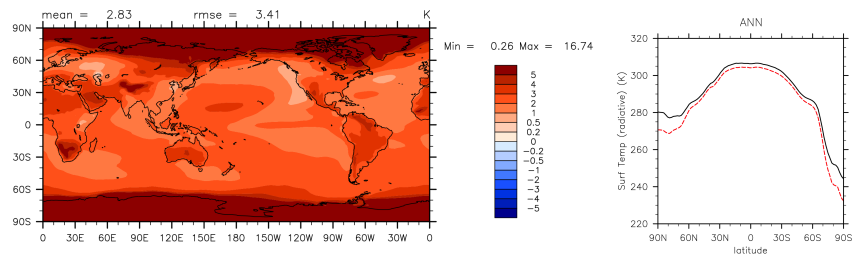


Figure 6.1.: Surface temperature difference plot for the modified SLF simulations minus their respective control simulations are shown in the horizontal contour plots on the left. The zonal mean plot for SLF simulations (black) and their respective control simulations (red dashed) is shown on the right.

When the modifications are added to the model, each simulation showed warming. As their  $\text{CO}_2$  amounts increased, the amount of warming from the control also in-

creased (Figure 6.2). After initial spin up, approximately 15 years, the pre-industrial modified simulation averages out to around 0°K of warming. The modern modified at 400 is approximately about 2.5 °K compared to the modern 400 control simulation warming about 2 °K. The modern at 800 ppm CO<sub>2</sub> modified simulation shoots up to about 7.5 degrees of warming compared to the control simulation showing approximately 5 degrees of warming from initial conditions (Figure 6.2).

### Change in Surface Temperature [K]

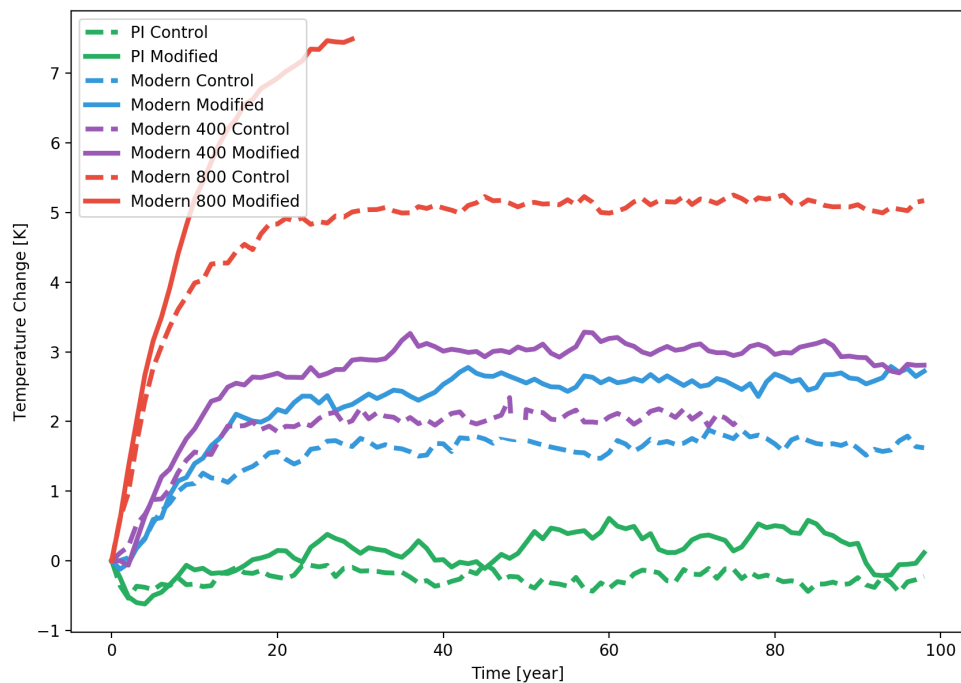


Figure 6.2.: Time series plot of change in surface temperature for all slab-ocean cases years 0-100.

Another representation of the temperature change across the versions of the modified model are seen when plotted as simulation temperature increases (Figure 6.3). Here it is easily shown that as CO<sub>2</sub> is increased in the modified simulations from 284.7 ppm to 800 ppm, the ending temperature of the model is increased from 289 K to 297 K. The best fit line is plotted between these three points, representing a nearly

linear response between total temperature change and ending average temperature of the model.

### Change in Surface Temperature [K] against Temperature

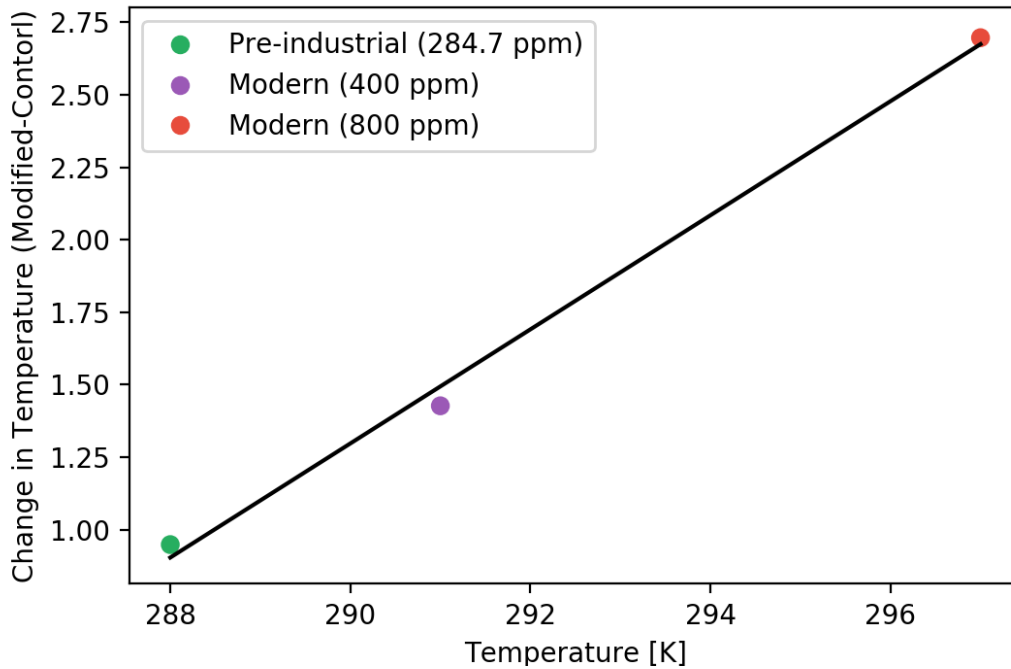


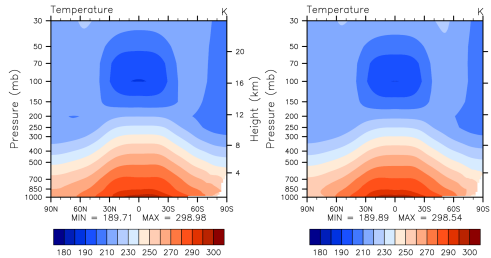
Figure 6.3.: Represents the change in temperature averaged for the last 10 years plotted against the temperature averaged for the last 10 years of each modified simulation.

Annual temperature vertical contour plots are shown in Figure 6.4. For each subplot a-d, the respective control case is to the right of the modified case and the difference between the control and modified simulations shown in the bottom plot. The amplified temperature at each pole can easily be seen in the difference plots for all simulations. As CO<sub>2</sub> increases in the simulations, the area of temperature increase is spread towards the equator and the middle atmosphere also increases in temperature. This can be seen predominantly in the bottom plot of section d. All four plots show similar patterns of warming and cooling. The near surface heating at the poles has an

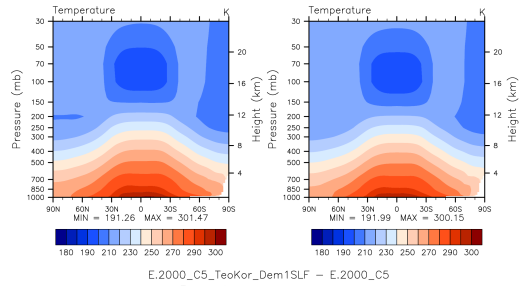
area of cooling at approximately 150 mb. Again, this cooling at 150 mb is amplified as CO<sub>2</sub> increases from pre-industrial to the modern 800 simulation.

### Temperature Vertical Contour Plots

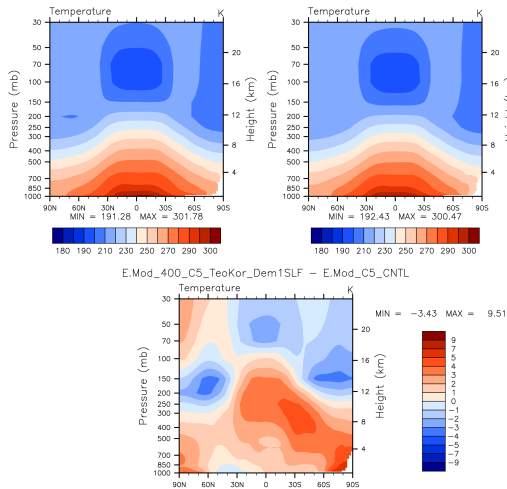
(a) PI simulation



(b) Modern simulation



(c) Modern 400 simulation



(d) Modern 800 simulation

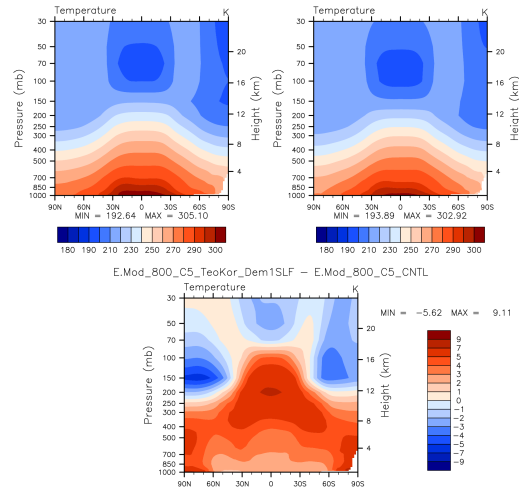


Figure 6.4.: Vertical contour plots of temperature [K] for the modified SLF simulations and their respective control simulations.

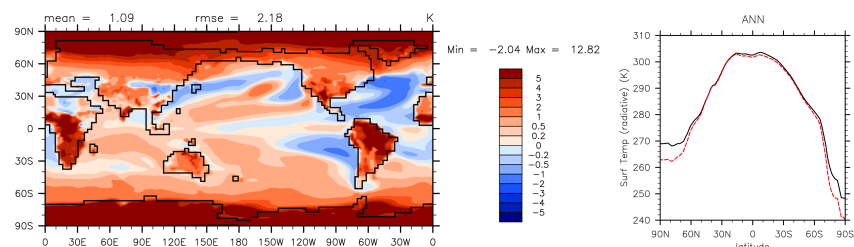
### 6.1.1 Miocene

Preliminary results for the Miocene fully-coupled simulations are showed and described below. These results are for the average of simulation years 1350-1360. Keep in mind that the cases below are not ran out far enough to make definitive conclusions, but show preliminary results. The simulations are appearing to continue to go the same direction as presented below. The comparison figures presented in this section are a) the Miocene at 400 CO<sub>2</sub> modified simulation minus the Miocene at 400 CO<sub>2</sub> control simulation, b) the Miocene at 800 CO<sub>2</sub> modified simulation minus the Miocene at 400 CO<sub>2</sub> control simulation, and c) the Miocene at 800 CO<sub>2</sub> modified simulation minus the Miocene at 400 CO<sub>2</sub> modified simulation. Unfortunately, a Miocene 800 CO<sub>2</sub> control simulation is not included in this study.

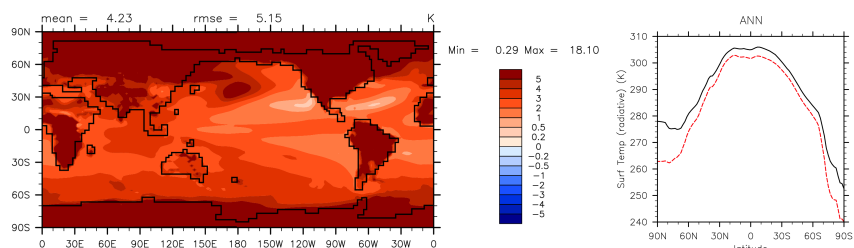
Figure 6.5 compares the average annual surface temperature for the Miocene simulations. Like in the modern cases, the modified simulations have an increase in surface temperature in the high latitudes. In Plot A, there is an increase in warming over land near the equator in the areas of Africa, South America, and northern Australia. As CO<sub>2</sub> is increased in the modified model, the warming is enhanced, notably in the arctic region seen in Plot C. There is an area of cooling off the coast of North America in the modified simulations at higher ppm CO<sub>2</sub>.

## Surface Temperature Difference

(a) Miocene 400 simulation (modified - control at 400)



(b) Miocene 800 simulation (modified - control at 400)



(c) Miocene 800 - Miocene 400 simulation

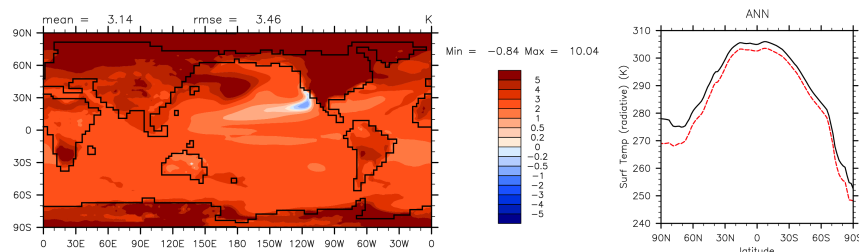


Figure 6.5.: Surface temperature difference plot for the modified SLF simulations are shown on the left. The zonal mean plot for SLF simulations (black) and reference simulations (red dashed) are on the right.

Vertical contour plots also show the weakening of the temperature gradient in the Miocene simulations (Figure 6.6). The bottom figures show the difference between the modified case and the control case. Red highlights the area of warming and blue highlights the areas of cooling in these figures. At 400 ppm, the area of greatest warming occurs over both of the poles near the surface, corresponding to the locations of warming found in previous figures for the pre-industrial and modern simulations (Figure 6.4). Again, as  $\text{CO}_2$  is increased, the warming and cooling intensifies in the modified simulations (Figure 6.6 Plot C).

## Temperature Vertical Contour Plots

(a) Miocene 400 simulation (b) Miocene 800 simulation (c) Miocene 800 - Miocene (modified - control at 400) (modified - control at 400) 400 simulation

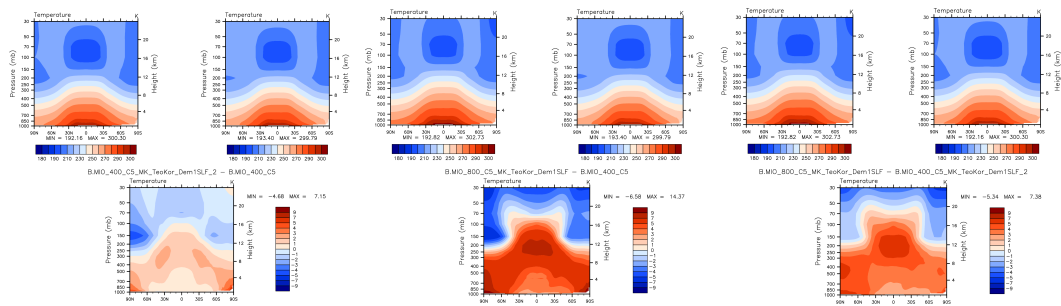


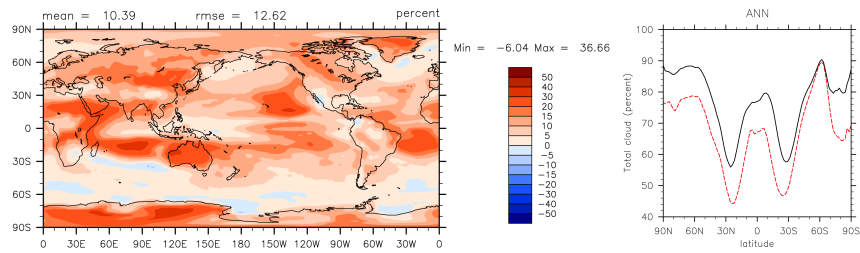
Figure 6.6.: Vertical contour plots of temperature for the modified SLF simulations and their respective control simulations.

## 6.2 Cloud Amount

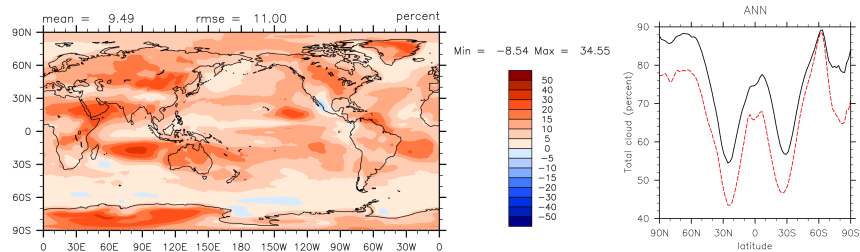
Figure 6.7 below shows the annual difference in total cloud amount in the models. Overall there is an increase in cloudiness all over the Earth in all modified simulations when compared with their control. Areas of Greenland, Antarctica, and Africa have consistent increase in clouds throughout each simulation. The zonal mean plots for each simulation show the separation from the black modified case line and the red control case line over all latitudes, again pointing towards an overall increase in cloudiness over the entire globe. These plots represent cloud amount for all levels of clouds. The next three plots breaks down cloud amount by high-level clouds, mid-level clouds, and low-level clouds.

## Total Cloud Amount Difference: Modified - Control

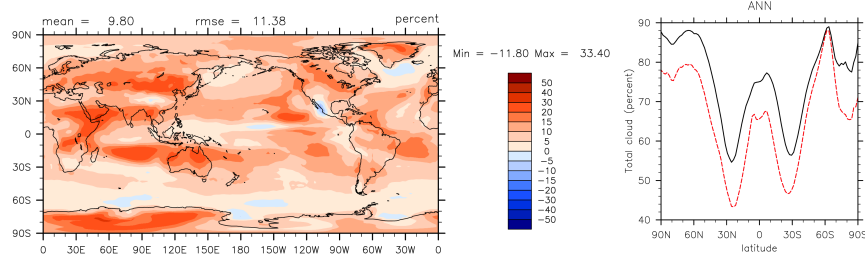
(a) PI simulation



(b) Modern simulation



(c) Modern 400 simulation



(d) Modern 800 simulation

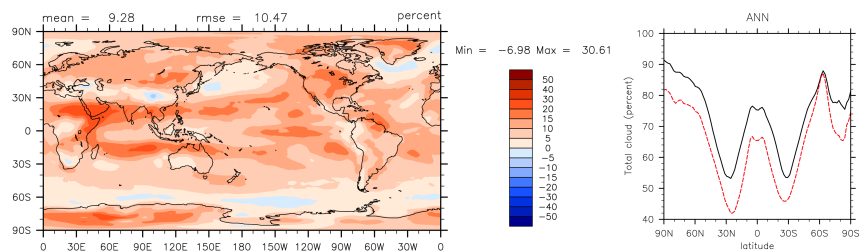


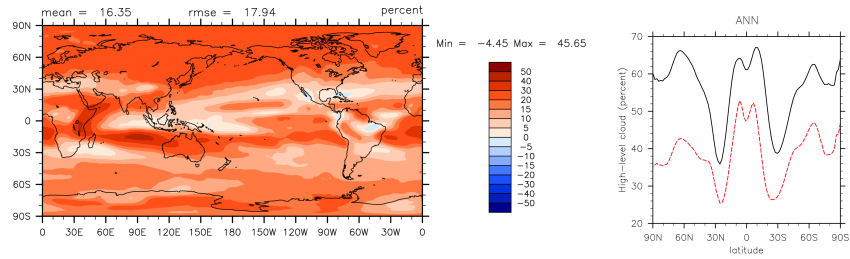
Figure 6.7.: Total cloud amount difference plot for the modified SLF simulations minus their respective control simulations are shown in the horizontal contour plots on the left. The zonal mean plot for SLF simulations (black) and their respective control simulations (red dashed) is shown on the right.

High-level cloud amount is described in Figure 6.8. In all simulations, an increase in high-level clouds are shown all over the globe. The zonal mean plots show a large

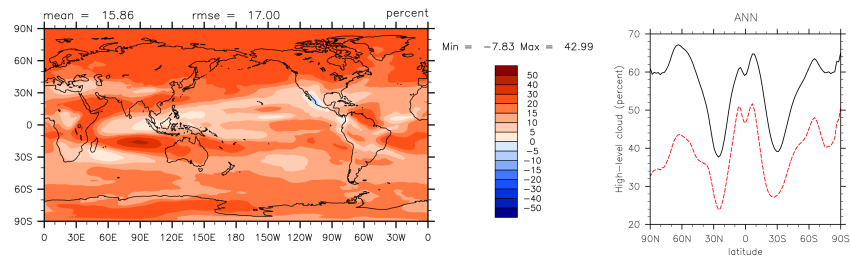
gap between the control and modified simulations across all latitudes. The greatest increase in high clouds occurs in arctic region and high latitudes to about 30°N. There is also a band across the equator of high-level cloud increase. The mean increase from control to modified simulation for pre-industrial is 15.35 percent, 15.86 percent for modern, 16.01 percent for modern at 400 CO<sub>2</sub>, and 15.07 percent for modern at 800 CO<sub>2</sub>, showing that the modifications made to the models might not be that sensitive to CO<sub>2</sub> when it comes to the high level clouds feedback.

## High-level Cloud Amount Difference: Modified - Control

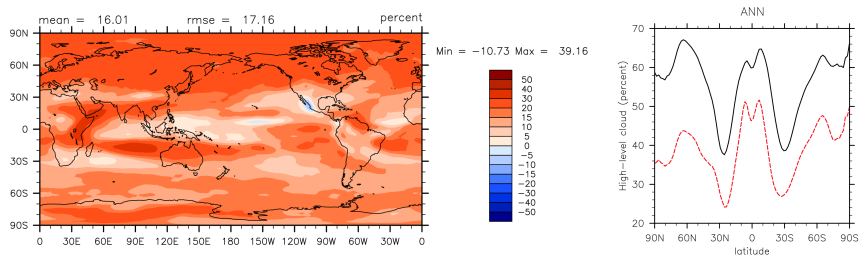
(a) PI simulation



(b) Modern simulation



(c) Modern 400 simulation



(d) Modern 800 simulation

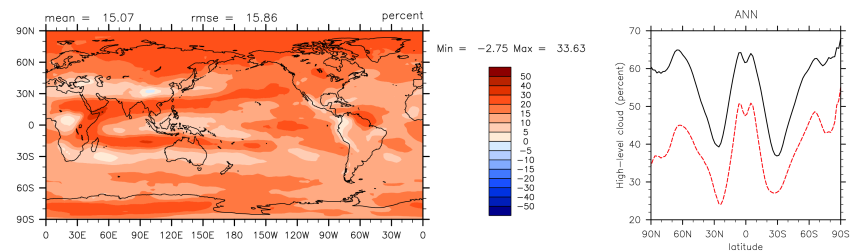


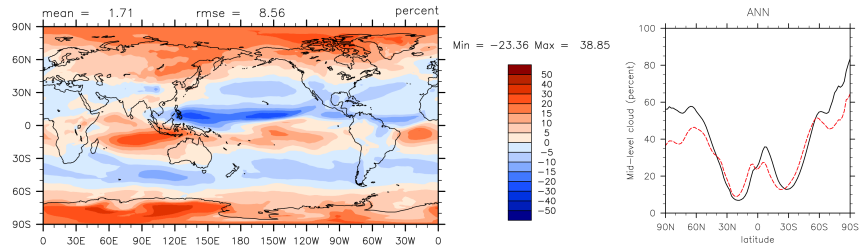
Figure 6.8.: High-level cloud amount difference plot for the modified SLF simulations minus their respective control simulations are shown in the horizontal contour plots on the left. The zonal mean plot for SLF simulations (black) and their respective control simulations (red dashed) is shown on the right.

Mid-level cloud amount's response to the modifications made to the simulations show more varied response compared to the high-level cloud amount. The pre-

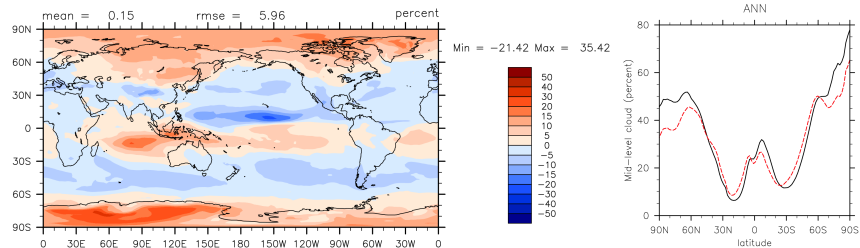
industrial, modern, and modern 400 simulations show increase in mid-level clouds in the high latitudes, both North and South, yet a slight decrease in the mid-latitude regions in Figure 6.9 below. The modern 800 simulation has an overall decrease in mid-level cloud amount, with a mean of -1.45 percent (decrease). At higher levels of CO<sub>2</sub>, plots a-c also show decreasing trend in mean mid-level cloud amount starting from 1.71 percent increase in the pre-industrial comparison to 0.15 and 0.21 percent increase in the modern and modern 400 simulations respectively. When looking at the zonal mean plots, there is a slight shift southward (right) of the black modified line when compared to the red control line. The overall shape, maximum and minimum mid-level cloud amounts, of the lines are similar with troughs in the mid-latitudes and peaks near the equator and higher latitudes.

## Mid-level Cloud Amount Difference: Modified - Control

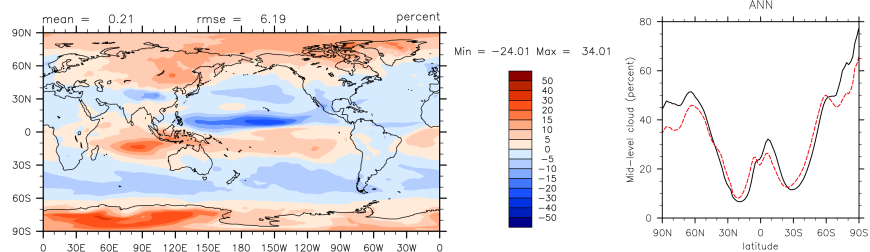
(a) PI simulation



(b) Modern simulation



(c) Modern 400 simulation



(d) Modern 800 simulation

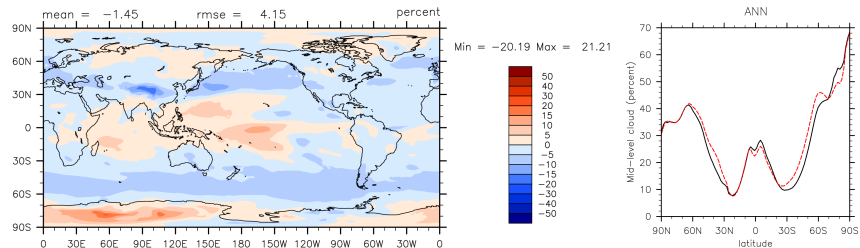


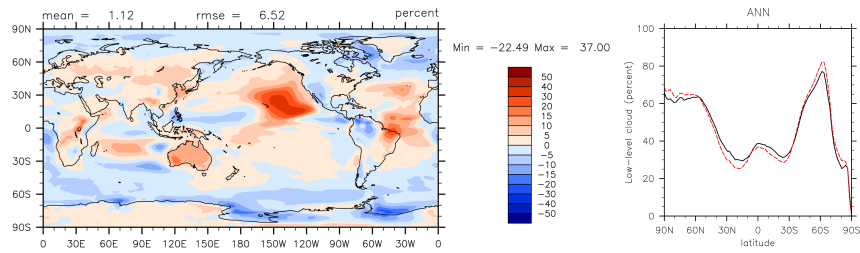
Figure 6.9.: Mid-level cloud amount difference plot for the modified SLF simulations minus their respective control simulations are shown in the horizontal contour plots on the left. The zonal mean plot for SLF simulations (black) and their respective control simulations (red dashed) is shown on the right.

Low-level cloud amount is shown in Figure 6.10. Looking at the zonal mean plots on the right, the red dashed control line and the black solid modified line are close

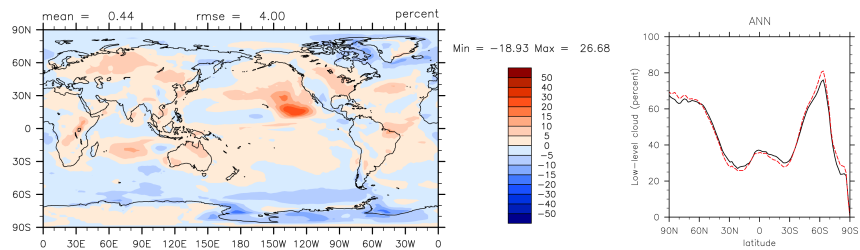
together and overlapping in most of the simulation sets. Increases and decreases in low-level cloud percentage are scattered across the globe and are relatively small compared to mid-level and high-level cloud amounts previously shown. Annual global mean values for the modified minus control cases are 1.12 percent, 0.44 percent, 0.66 percent, and 0.19 percent for the pre-industrial, modern, modern 400, and modern 800 simulations. These values decrease slightly as CO<sub>2</sub> increases across the cases from 284.7 ppm to 800.0 ppm.

## Low-level Cloud Amount Difference: Modified - Control

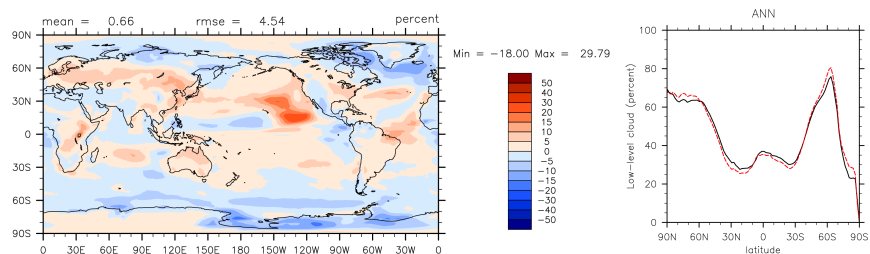
(a) PI simulation



(b) Modern simulation



(c) Modern 400 simulation



(d) Modern 800 simulation

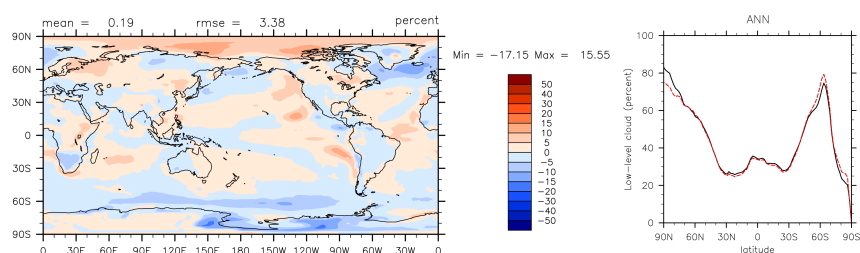


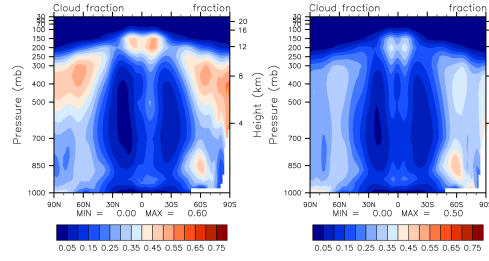
Figure 6.10.: Low-level cloud amount difference plot for the modified SLF simulations minus their respective control simulations are shown in the horizontal contour plots on the left. The zonal mean plot for SLF simulations (black) and their respective control simulations (red dashed) is shown on the right.

As previous figures showed, an increase in high clouds are expected in the modified versions of the model. The bottom figures in every subplot agree with this. They have

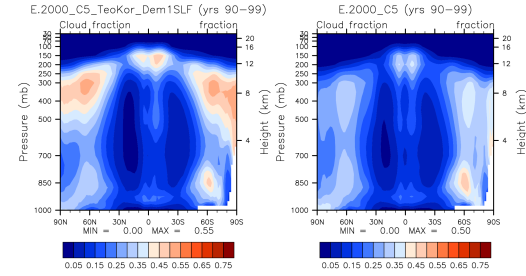
an increase in clouds from about 300 mb over the poles to 150 mb over the equator. As CO<sub>2</sub> increases from pre-industrial simulations to modern 800 simulations, the area of maximum cloud increase condenses yet has a stronger increase when compared to the control case. The pre-industrial has a spread of cloud increase at 500 to 200 mb over the North Pole. The modern 800 simulation has a spread of cloud increase at 400 to 200 mb. All modified models have a maximum cloud total increase of about 20 percent.

## Total Cloud Amount Vertical Contour Plots

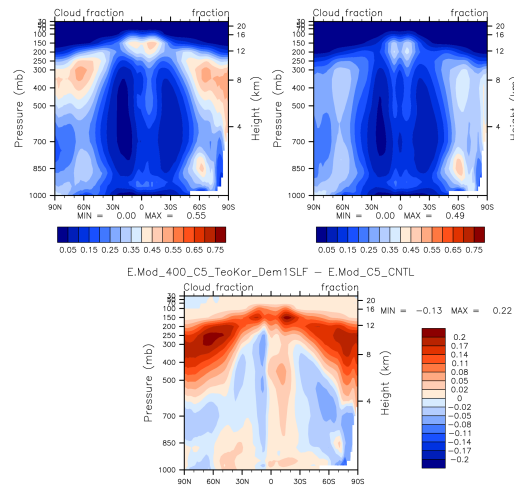
(a) PI simulation



(b) Modern simulation



(c) Modern 400 simulation



(d) Modern 800 simulation

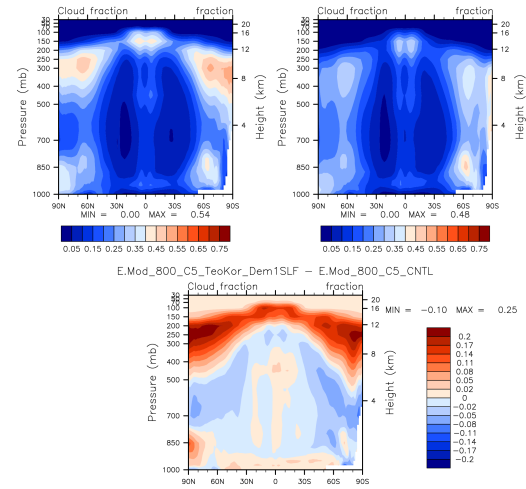


Figure 6.11.: Vertical contour plots of total cloud amount for the modified SLF simulations and their respective control simulations.

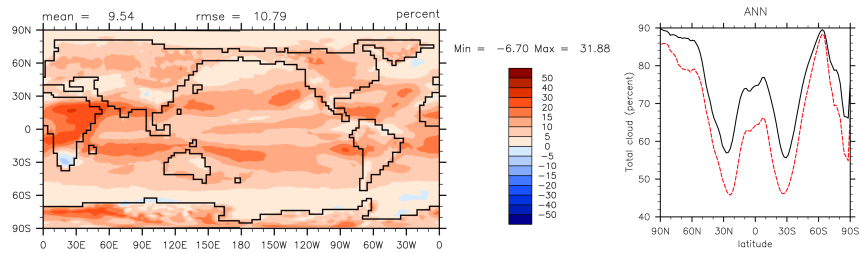
### 6.2.1 Miocene

Total cloud amount is compared in the control simulation at 400 CO<sub>2</sub> with the modified simulations at 400 and 800 CO<sub>2</sub>. As anticipated from the pre-industrial and modern results, the Miocene also shows an overall increase in cloudiness throughout the entire globe. Areas of greater cloud percentage is centered around the equator,

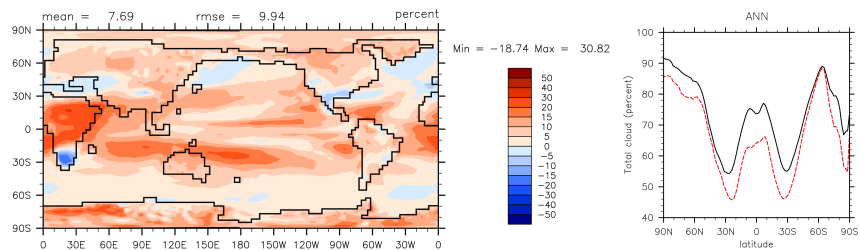
seen in the 400 ppm case. Although, when comparing the 400 to the 800 ppm CO<sub>2</sub>, there is little to less amount of clouds in the simulations with higher carbon dioxide concentrations.

### Total Cloud Amount Difference

(a) Miocene 400 simulation (modified - control at 400)



(b) Miocene 800 simulation (modified - control at 400)



(c) Miocene 800 - Miocene 400 simulation

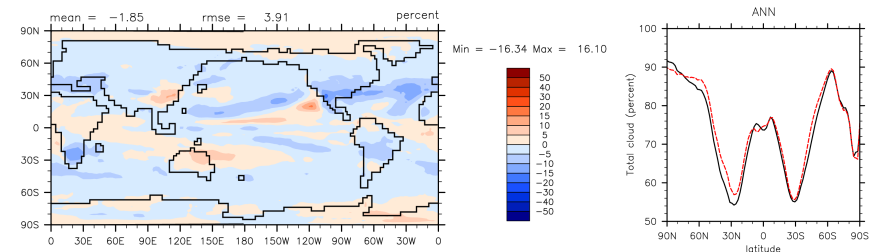
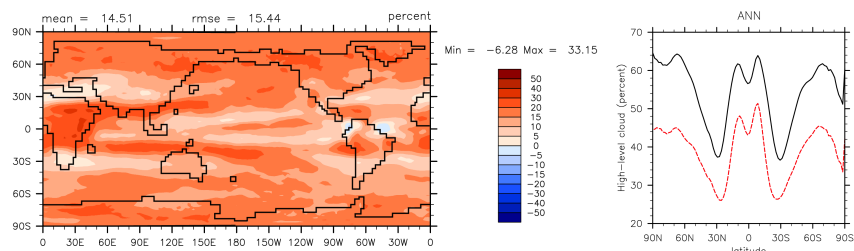


Figure 6.12.: Total cloud amount difference plot for the modified SLF simulations are shown on the left. The zonal mean plot for SLF simulations (black) and reference simulations (red dashed) are on the right.

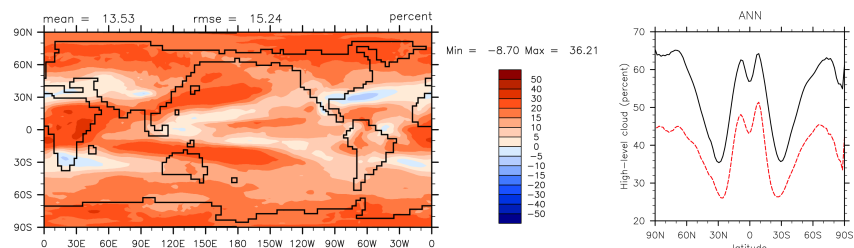
The biggest increase in total cloud percentage comes from the increase in high clouds in the model. Overall, high clouds in the modified simulations are increased across the entire globe. As in total cloudiness, the increase in greenhouse gas does not increase the average high cloud percentage in the simulations, there is an average decrease of 0.98 percent (Figure 6.13 Plot C).

## High-level Cloud Amount Difference

(a) Miocene 400 simulation (modified - control at 400)



(b) Miocene 800 simulation (modified - control at 400)



(c) Miocene 800 - Miocene 400 simulation

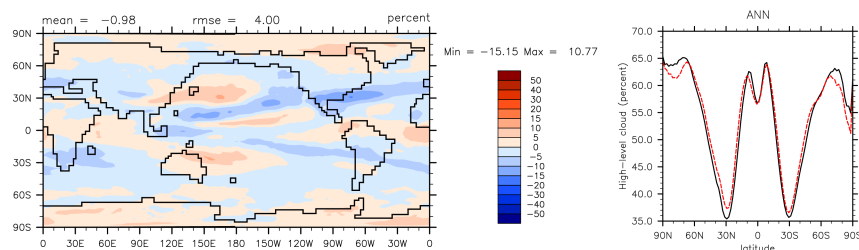
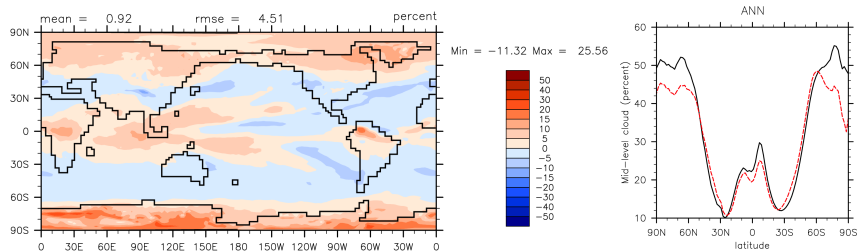


Figure 6.13.: High-level cloud amount difference plot for the modified SLF simulations are shown on the left. The zonal mean plot for SLF simulations (black) and reference simulations (red dashed) are on the right.

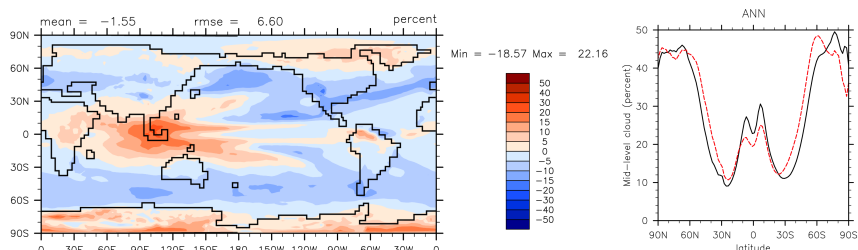
Mid-level clouds are slightly greater in the 400 ppm modified Miocene simulation when compared to the control. The greatest areas of increase are in the high latitudes and centered around the equator (Figure 6.14). As in the high cloud comparison of 800 ppm to 400 ppm  $\text{CO}_2$ , the average mid-level clouds actually decrease in the modified simulations at higher concentrations. This result is also seen in the modern and pre-industrial modified simulations (Figure 6.9).

## Mid-level Cloud Amount Difference

(a) Miocene 400 simulation (modified - control at 400)



(b) Miocene 800 simulation (modified - control at 400)



(c) Miocene 800 - Miocene 400 simulation

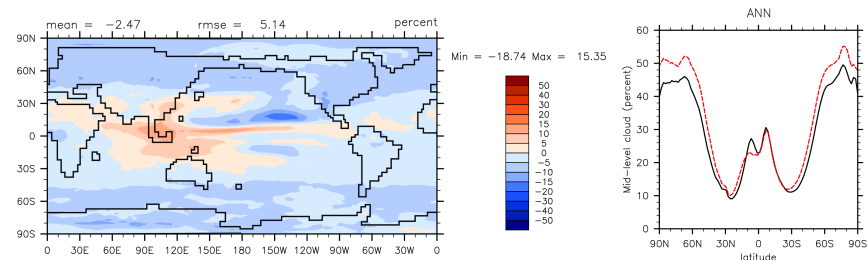
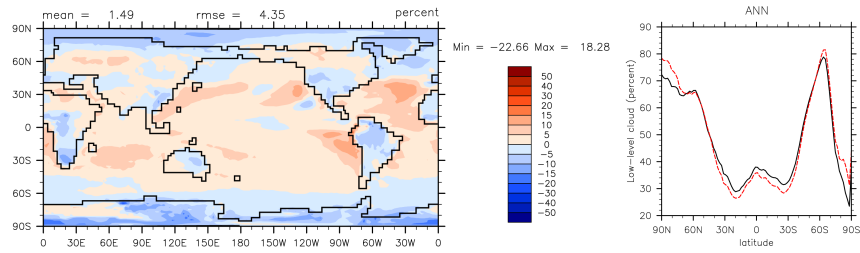


Figure 6.14.: Mid-level cloud amount difference plot for the modified SLF simulations are shown on the left. The zonal mean plot for SLF simulations (black) and reference simulations (red dashed) are on the right.

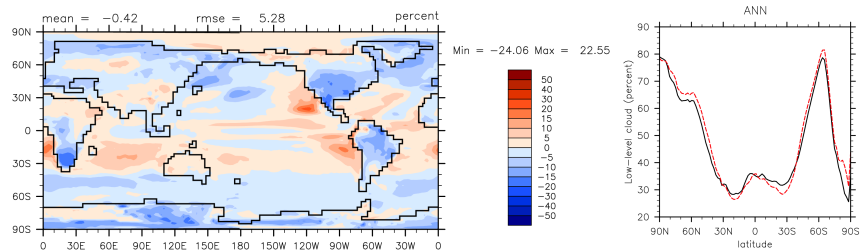
It has already been shown that the greatest increase in total cloud fraction comes from the increase in high level clouds (Figure 6.13), but on average the low level clouds represented in the modified simulations decrease in the high latitudes when compared to the control simulation (Figure 6.15). Again at higher values of  $\text{CO}_2$ , there is less low-cloud coverage in most areas of the globe. In the zonal mean comparisons between 400 and 800 ppm, both simulations follow the same curve with more variability in the Northern high latitudes and only slight deviations from each other across the other latitudes.

## Low-level Cloud Amount Difference

(a) Miocene 400 simulation (modified - control at 400)



(b) Miocene 800 simulation (modified - control at 400)



(c) Miocene 800 - Miocene 400 simulation

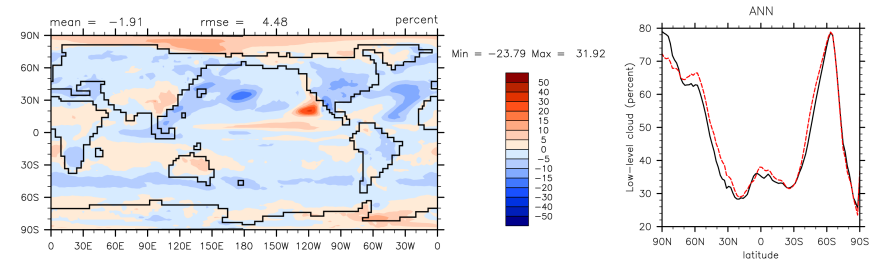


Figure 6.15.: Low-level cloud amount difference plot for the modified SLF simulations are shown on the left. The zonal mean plot for SLF simulations (black) and reference simulations (red dashed) are on the right.

## Total Cloud Amount Vertical Contour Plots

(a) Miocene 400 simulation (b) Miocene 800 simulation (c) Miocene 800 - Miocene 400 (modified - control at 400) (modified - control at 400) 400 simulation

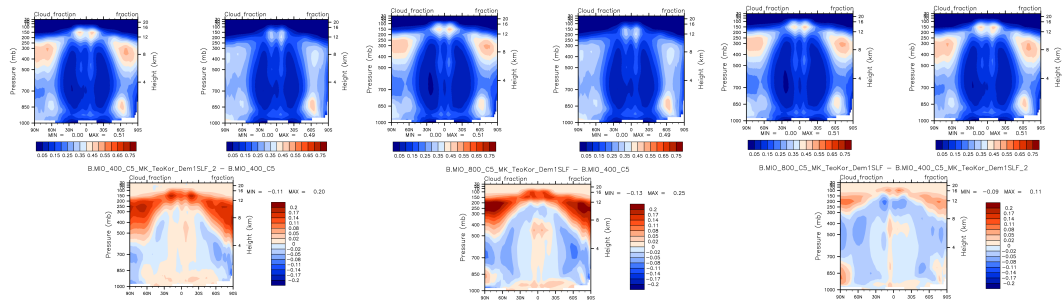


Figure 6.16.: Vertical contour plots of total cloud amount for the modified SLF simulations and their respective control simulations.

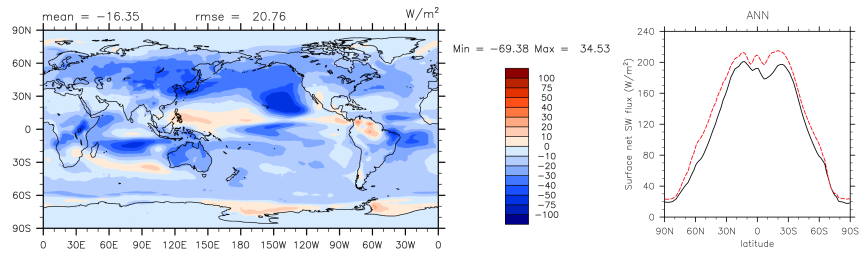
The following figures look at the difference in net longwave and shortwave fluxes at the top of the model and at the surface.

### 6.3 Fluxes

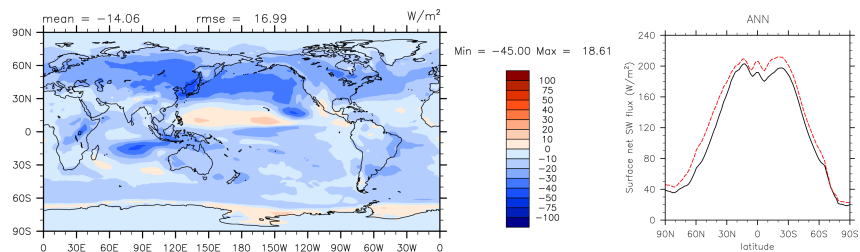
Figure 6.17 shows the surface net shortwave flux difference from the control to modified cases for pre-industrial, modern, modern at 400 ppm CO<sub>2</sub>, and modern at 800 ppm CO<sub>2</sub> in plots a-d. All graphs show a mean decrease in surface shortwave flux, yet at higher values of CO<sub>2</sub> the decrease is lessened. Across all latitudes, seen in the zonal mean plots on the right side, surface net shortwave flux is less in the modified case than the control. Next, the surface longwave net flux is plotted.

## Surface Net Shortwave Flux Difference: Modified - Control

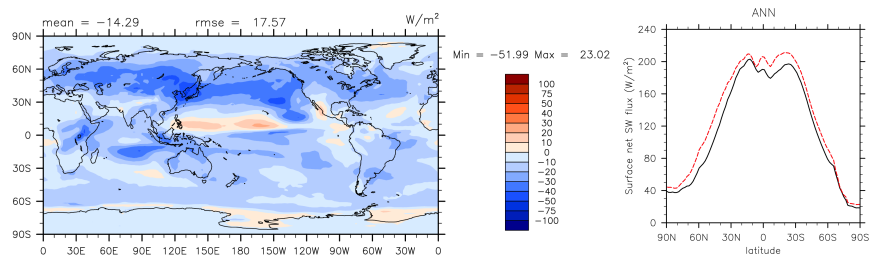
(a) PI simulation



(b) Modern simulation



(c) Modern 400 simulation



(d) Modern 800 simulation

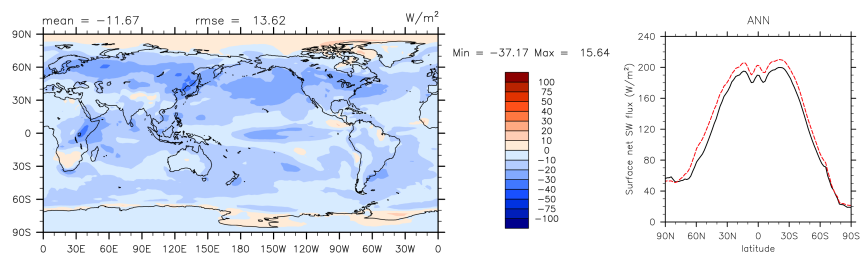


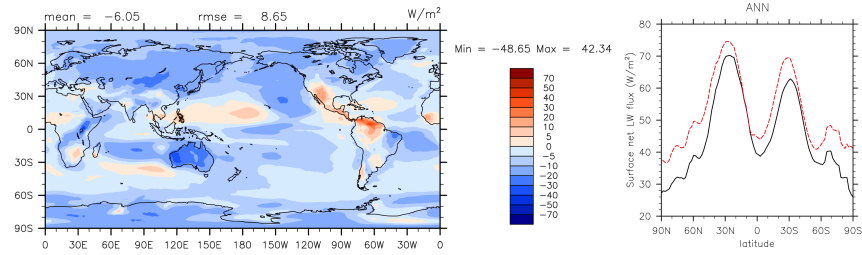
Figure 6.17.: Surface net shortwave flux difference plot for the modified SLF simulations minus their respective control simulations are shown in the horizontal contour plots on the left. The zonal mean plot for SLF simulations (black) and their respective control simulations (red dashed) is shown on the right.

Below in Figure 6.18, the difference in net longwave flux at the surface is plotted for each simulation. Like the shortwave flux, there is a decrease in surface longwave

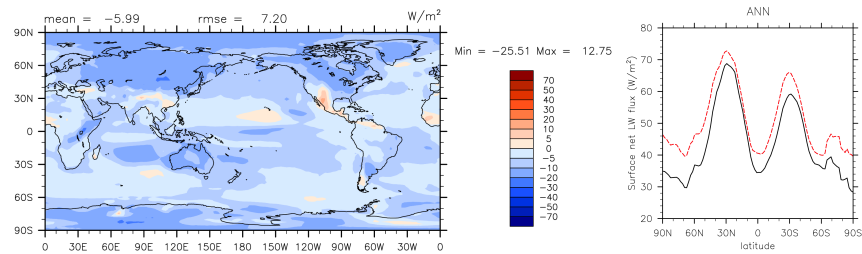
flux in the modified case. With values of -6.05, -5.09, -6.02, and -6.15 W/m<sup>2</sup>, the increase in CO<sub>2</sub> does not appear to affect the magnitude of change in global mean surface net longwave flux from the modifications. The shapes for the zonal mean plots are all similar with slight differences in the values. Both the shortwave and longwave net surface fluxes are decreasing in the modified versions of the model. Next, the top of atmosphere longwave and shortwave net fluxes are presented.

## Surface Net Longwave Flux Difference: Modified - Control

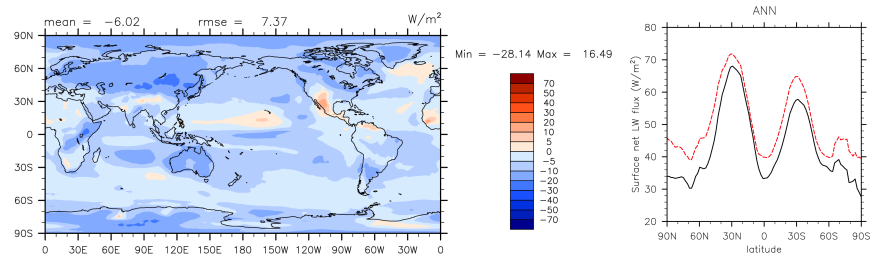
(a) PI simulation



(b) Modern simulation



(c) Modern 400 simulation



(d) Modern 800 simulation

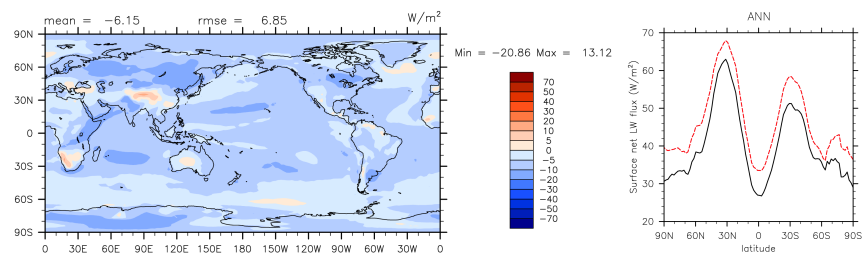


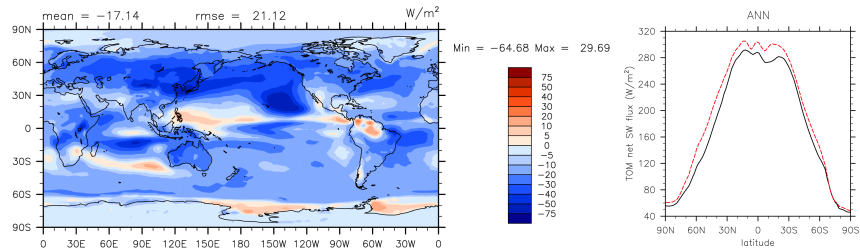
Figure 6.18.: Surface net longwave flux difference plot for the modified SLF simulations minus their respective control simulations are shown in the horizontal contour plots on the left. The zonal mean plot for SLF simulations (black) and their respective control simulations (red dashed) is shown on the right.

Figure 6.18, there is a large decrease in top of model net shortwave flux when modifications are made to the model. This decrease is seen across all simulations,

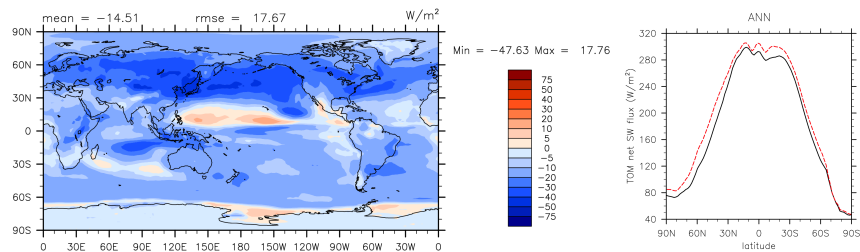
with the largest region of decrease occurring in the mid-latitudes. When CO<sub>2</sub> is at 800 ppm in plot d, there is a slight increase from the modified to the control in the arctic region. This same slight increase in the arctic region was seen on the surface net shortwave flux in the modern 8000 simulation in Figure 6.17.

## Top of Model Net Shortwave Flux Difference: Modified - Control

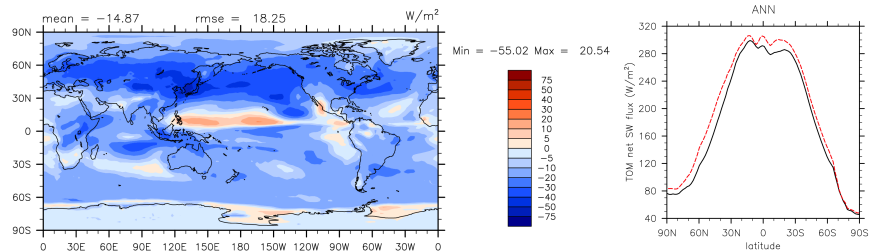
(a) PI simulation



(b) Modern simulation



(c) Modern 400 simulation



(d) Modern 800 simulation

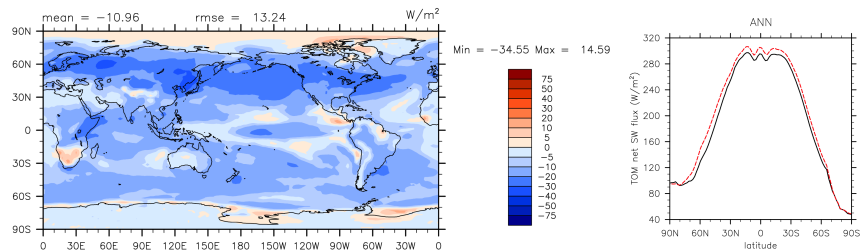


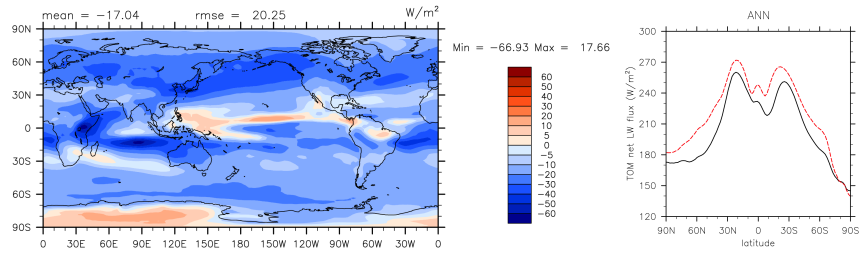
Figure 6.19.: Top of model net shortwave flux difference plot for the modified SLF simulations minus their respective control simulations are shown in the horizontal contour plots on the left. The zonal mean plot for SLF simulations (black) and their respective control simulations (red dashed) is shown on the right.

The top of model net longwave flux difference plots are presented below in Figure 6.20. Like the previous three figures, there is a mean decrease for all four simulations.

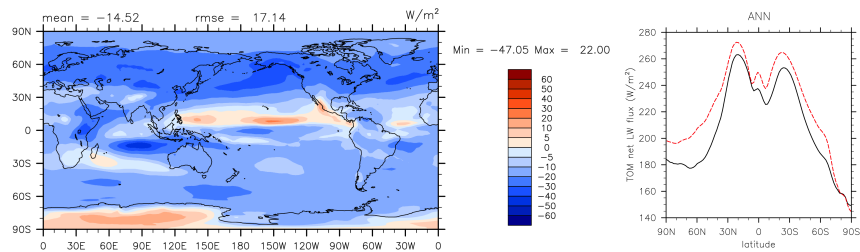
Although in this figure, an increase from the control to the modified cases is seen on the continent of Antarctica. In the cases with lower CO<sub>2</sub>, plots a-c, there is a strip of increase in net longwave flux at the top of model over the Pacific Ocean in the low northern latitudes, yet it disappears in the case with 800 ppm CO<sub>2</sub>. This can be seen in the horizontal contour maps as well as in the zonal mean line plots where the black modified simulation line is closer to the red control case line in the low north latitudes.

## Top of Model Net Longwave Flux Difference: Modified - Control

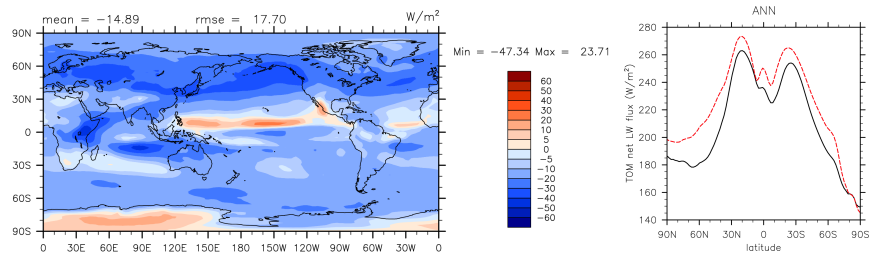
(a) PI simulation



(b) Modern simulation



(c) Modern 400 simulation



(d) Modern 800 simulation

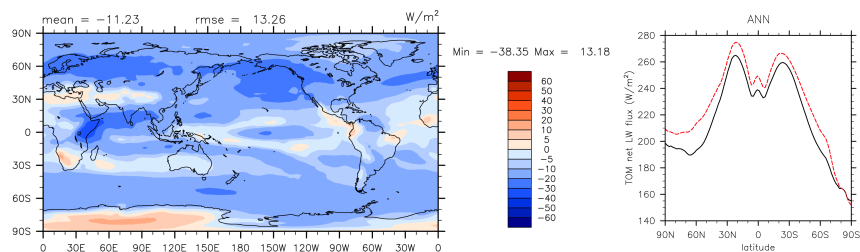


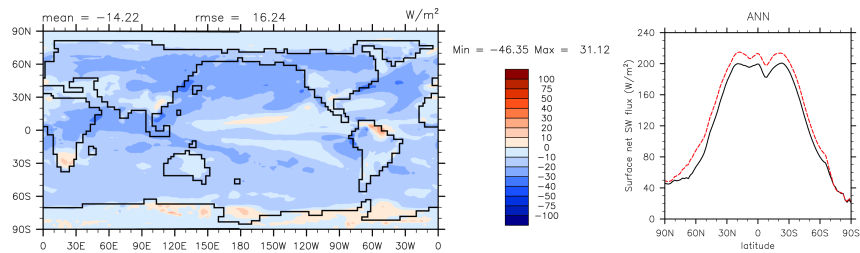
Figure 6.20.: Top of model net longwave flux difference plot for the modified SLF simulations minus their respective control simulations are shown in the horizontal contour plots on the left. The zonal mean plot for SLF simulations (black) and their respective control simulations (red dashed) is shown on the right.

### 6.3.1 Miocene

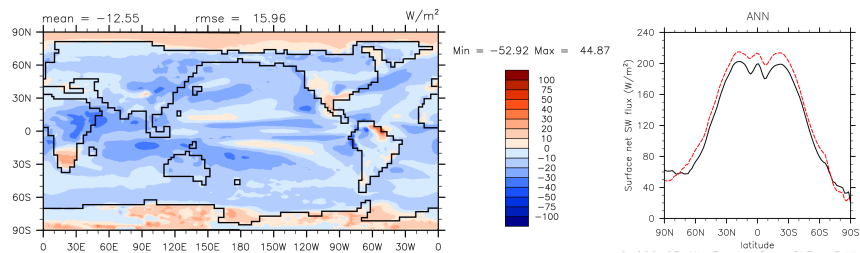
Overall, net shortwave flux at the surface decreases with the modifications included in the model (Figure 6.21). This decrease is maximized at the lower CO<sub>2</sub> simulation. Yet when comparing the change in surface net shortwave flux between 800 ppm and 400 ppm, there is an average increase in the 800 ppm case with the area of maximum increase in the high latitudes (Figure 6.21 Plot C).

#### Surface Net Shortwave Flux Difference

(a) Miocene 400 simulation (modified - control at 400)



(b) Miocene 800 simulation (modified - control at 400)



(c) Miocene 800 - Miocene 400 simulation

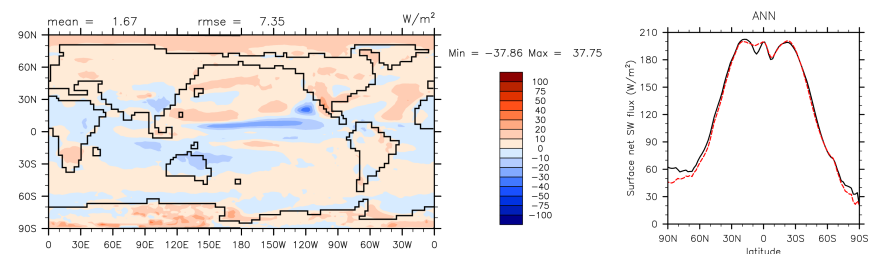
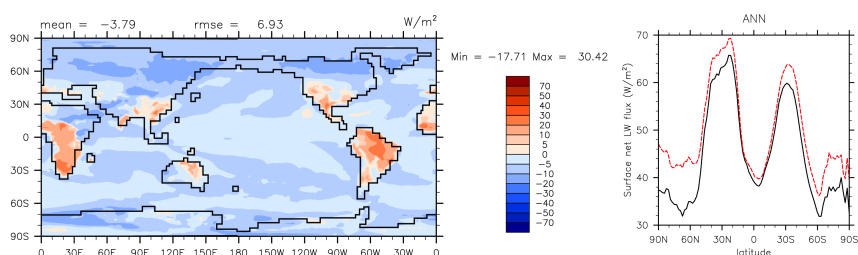


Figure 6.21.: Surface net shortwave flux difference plot for the modified SLF simulations are shown on the left. The zonal mean plot for SLF simulations (black) and reference simulations (red dashed) are on the right.

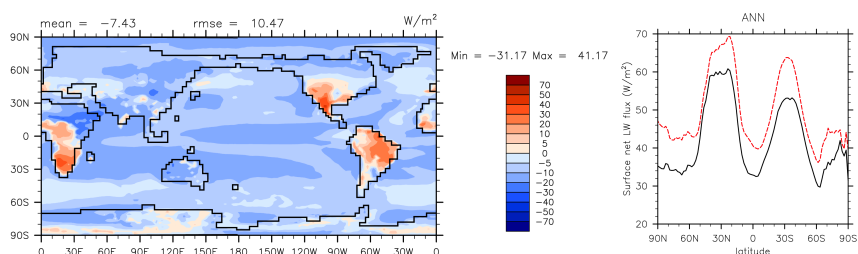
Surface net longwave flux also decreases in the modified versions of the model (Figure 6.22). This time as  $\text{CO}_2$  values increase, there is a greater decrease in the longwave surface flux. Areas of higher decrease in Miocene surface net longwave flux occur over the high latitudes, yet there are areas of strong net flux increase over Southern Africa, South America, and south parts of North America and these areas are slightly amplified at higher values of carbon dioxide (Figure 6.22).

### Surface Net Longwave Flux Difference

(a) Miocene 400 simulation (modified - control at 400)



(b) Miocene 800 simulation (modified - control at 400)



(c) Miocene 800 - Miocene 400 simulation

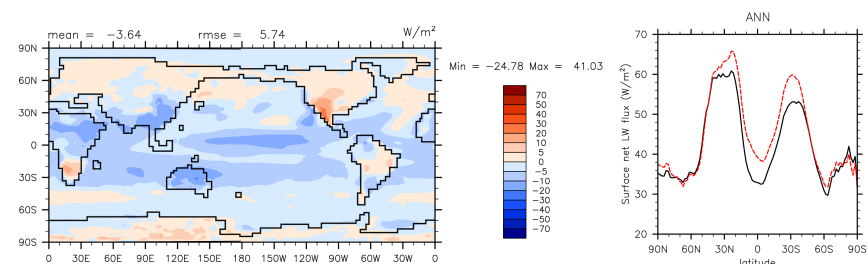


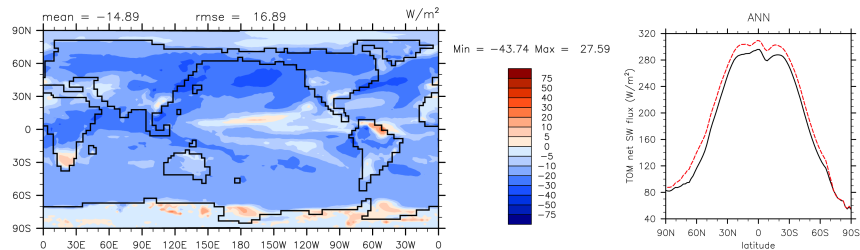
Figure 6.22.: Surface net longwave flux difference plot for the modified SLF simulations are shown on the left. The zonal mean plot for SLF simulations (black) and reference simulations (red dashed) are on the right.

The top of model fluxes show similar results as the surface fluxes with an overall decrease in both longwave and shortwave flux across the globe (Figure 6.23 and 6.24).

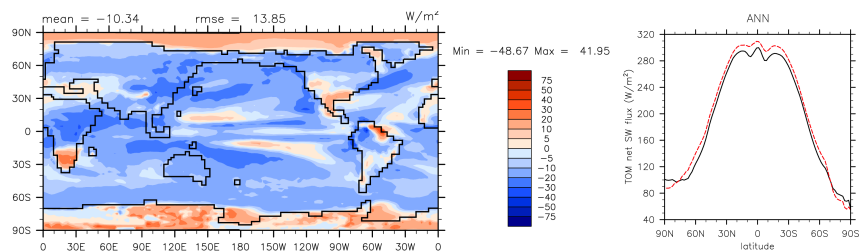
Along with the overall decrease in flux, there are two areas showing increases in top of model net shortwave flux at the Southern tip of Africa and Northeast corner of South America (Figure 6.23 Plot A). A doubling of  $\text{CO}_2$  in the modified simulations also increases the top of model net shortwave flux across the globe with a mean of  $4.55 \text{ W/m}^2$  and is strongest at the high latitudes (Figure 6.23 Plot C).

### Top of Model Net Shortwave Flux Difference

(a) Miocene 400 simulation (modified - control at 400)



(b) Miocene 800 simulation (modified - control at 400)



(c) Miocene 800 - Miocene 400 simulation

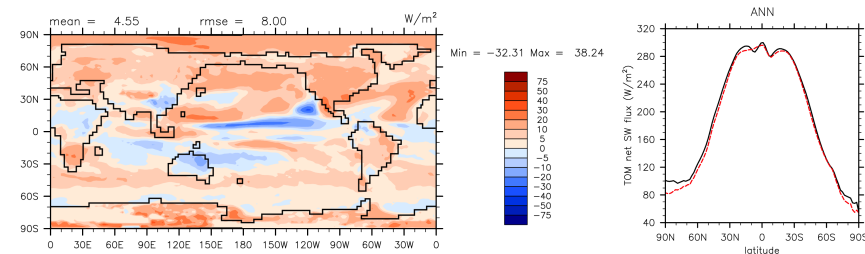


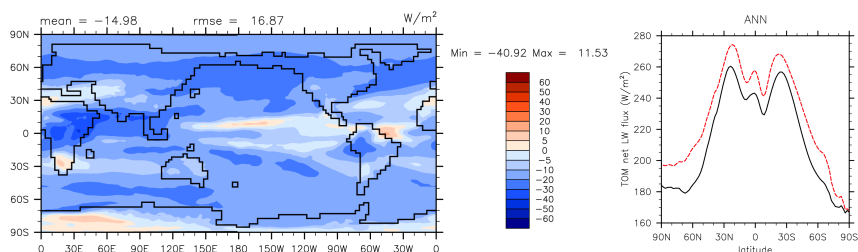
Figure 6.23.: Top of model net shortwave flux difference plot for the modified SLF simulations are shown on the left. The zonal mean plot for SLF simulations (black) and reference simulations (red dashed) are on the right.

Net longwave flux at the top of the model decreases across the planet in the modified simulations. Doubling of carbon dioxide in the modified cases leads to an

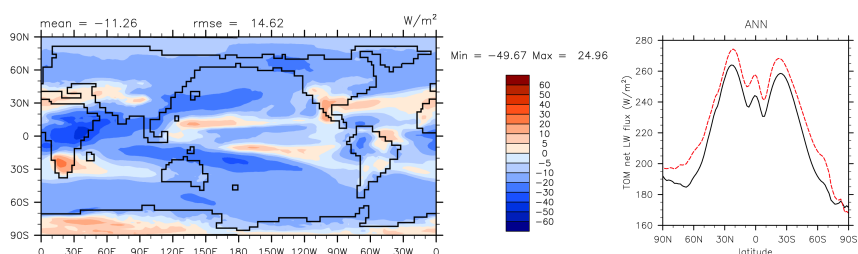
increase (approximately  $3.72 \text{ W/m}^2$  in the top of model net longwave flux and areas of maximum increase are located across the high latitudes (Figure 6.24 Plot C).

### Top of Model Net Longwave Flux Difference

(a) Miocene 400 simulation (modified - control at 400)



(b) Miocene 800 simulation (modified - control at 400)



(c) Miocene 800 - Miocene 400 simulation

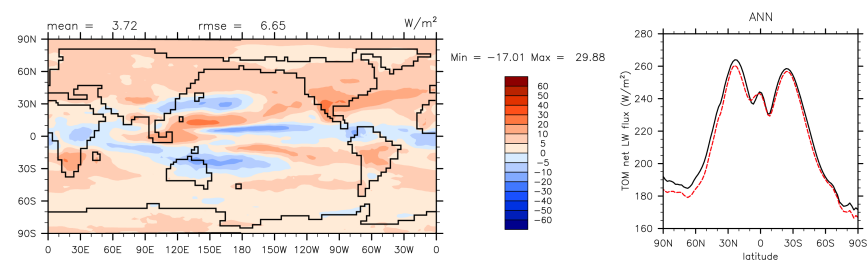


Figure 6.24.: Top of model net longwave flux difference plot for the modified SLF simulations are shown on the left. The zonal mean plot for SLF simulations (black) and reference simulations (red dashed) are on the right.

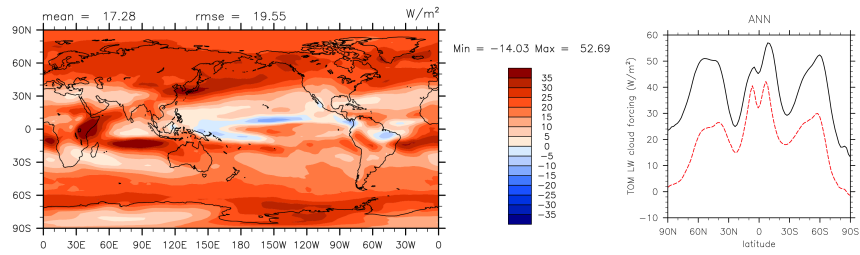
## 6.4 Cloud Forcing

The difference in longwave cloud forcing from the modified simulations and control simulations are represented in Figure 6.25. For every simulation there is an average increase in longwave cloud forcing in the modified case. With lower the  $\text{CO}_2$ , a larger increase is seen. Values of  $17.28 \text{ W/m}^2$ ,  $16.22 \text{ W/m}^2$ ,  $16.35 \text{ W/m}^2$ , and  $14.88 \text{ W/m}^2$

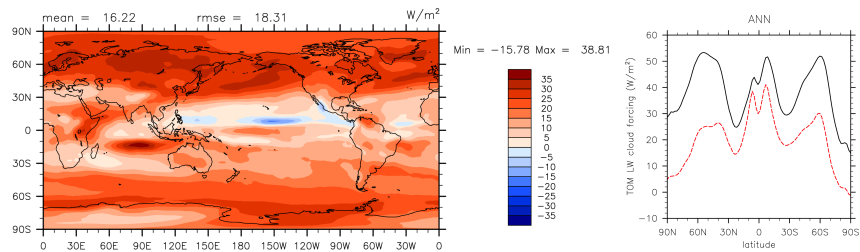
for the pre-industrial, modern, modern 400 CO<sub>2</sub>, and modern 800 CO<sub>2</sub>, were calculated. All plots represent the maximum increase in the arctic region, reaching down to approximately 30°N. The zonal mean plots on the right side also show the maximum difference occurring in the high northern hemisphere. Both lines, the control and modified, follow a similar shape across the latitudes with the black modified line at higher values of longwave cloud forcing.

## Longwave Cloud Forcing Difference: Modified - Control

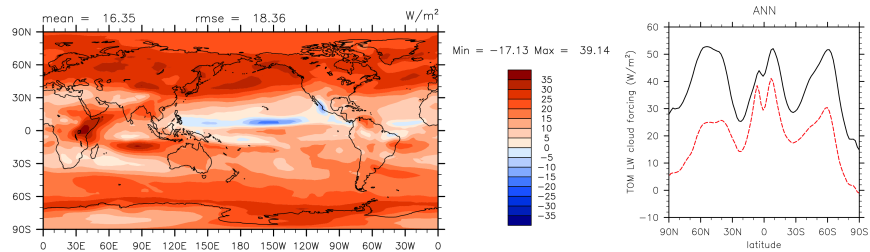
(a) PI simulation



(b) Modern simulation



(c) Modern 400 simulation



(d) Modern 800 simulation

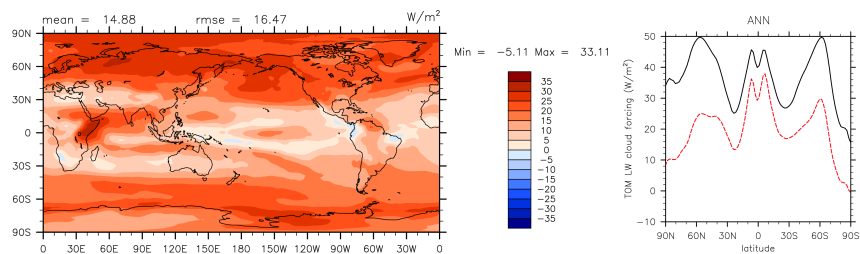


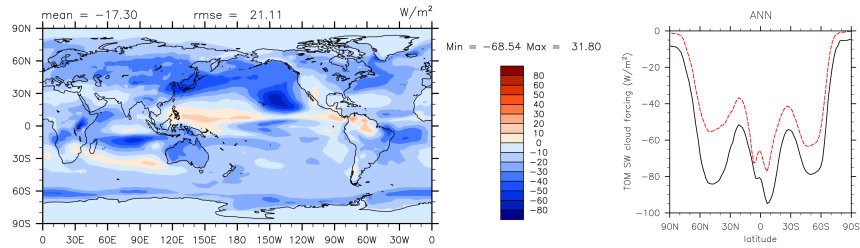
Figure 6.25.: Longwave cloud forcing difference plot for the modified SLF simulations minus their respective control simulations are shown in the horizontal contour plots on the left. The zonal mean plot for SLF simulations (black) and their respective control simulations (red dashed) is shown on the right.

Next, the difference in shortwave cloud forcing is shown below in Figure 6.26. As anticipated, there is an overall decrease from control to modified cases across

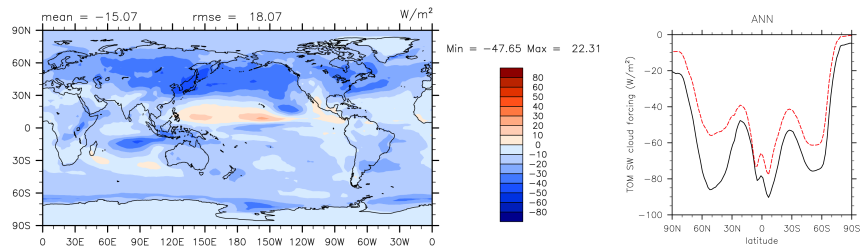
the globe. The pre-industrial case has the largest annual mean decrease of  $-17.30 \text{ W/m}^2$ . The modern high  $\text{CO}_2$  case has the decrease between control and modified at  $-12.41 \text{ W/m}^2$ . It appears that the area with the most decrease is in the northern mid-latitudes over the Pacific Ocean, yet this region of lower shortwave cloud forcing dissipates in the 800 ppm simulations. In the pre-industrial simulation the minimum difference value is  $-68.54 \text{ W/m}^2$  and in the modern 800 simulation the minimum difference value is only  $-35.06 \text{ W/m}^2$ . Therefore, at higher values of  $\text{CO}_2$  there is weaker shortwave cloud forcing when the modifications are implemented in the model.

## Shortwave Cloud Forcing Difference: Modified - Control

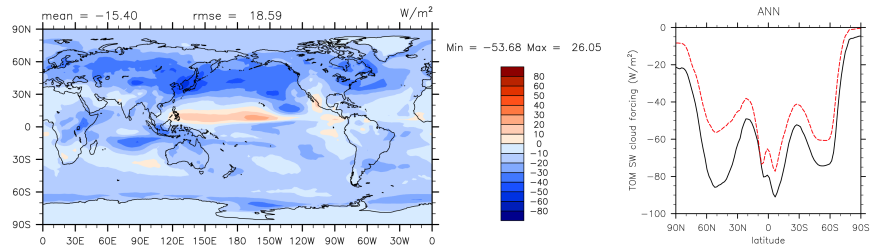
(a) PI simulation



(b) Modern simulation



(c) Modern 400 simulation



(d) Modern 800 simulation

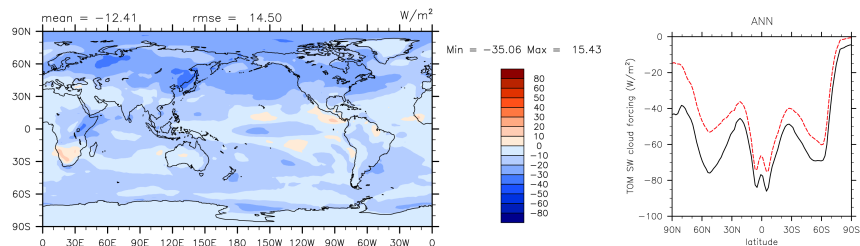


Figure 6.26.: Shortwave cloud forcing difference plot for the modified SLF simulations minus their respective control simulations are shown in the horizontal contour plots on the left. The zonal mean plot for SLF simulations (black) and their respective control simulations (red dashed) is shown on the right.

## Change in Cloud Forcing

(a) Shortwave Cloud Forcing

(b) Longwave Cloud Forcing

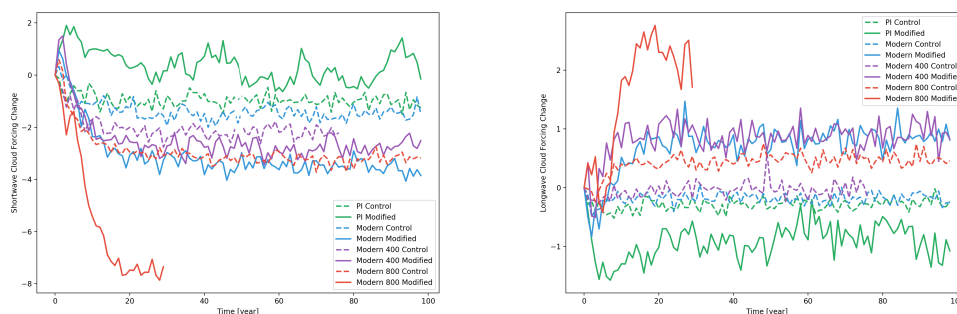


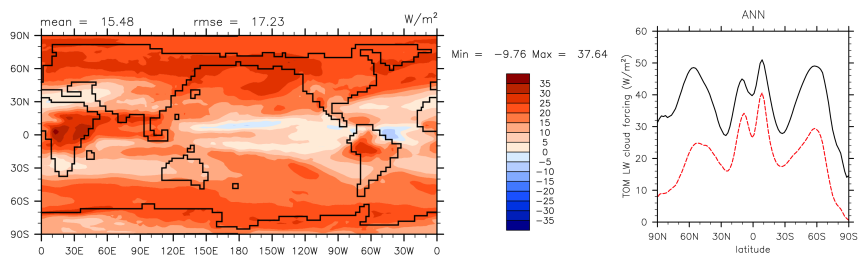
Figure 6.27.: Time series plots of shortwave cloud forcing and longwave cloud forcing across modified and control simulations.

### 6.4.1 Miocene

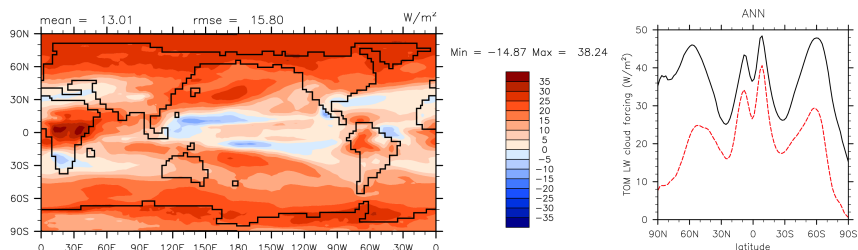
Longwave cloud forcing changes drastically with the modifications made to the model in the Miocene. An increase of  $15.48 \text{ W/m}^2$  is calculated when comparing the modified simulation to the control simulation at 400 ppm  $\text{CO}_2$  (Figure 6.28). Across all latitudes and longitudes there is an increase in longwave cloud forcing for both 800 and 400 ppm modified simulations.

## Longwave Cloud Forcing Difference

(a) Miocene 400 simulation (modified - control at 400)



(b) Miocene 800 simulation (modified - control at 400)



(c) Miocene 800 - Miocene 400 simulation

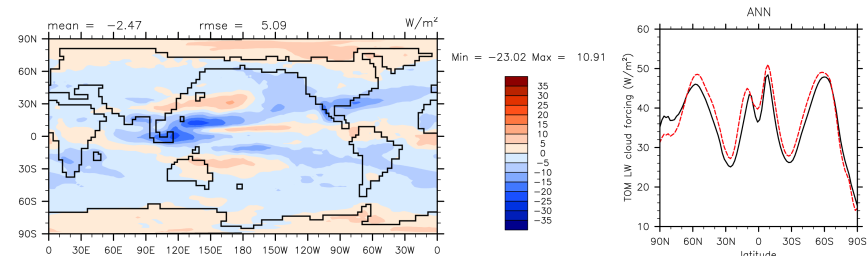
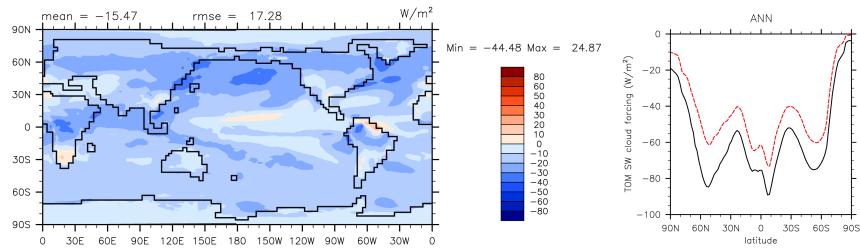


Figure 6.28.: Longwave cloud forcing difference plot for the modified SLF simulations are shown on the left. The zonal mean plot for SLF simulations (black) and reference simulations (red dashed) are on the right.

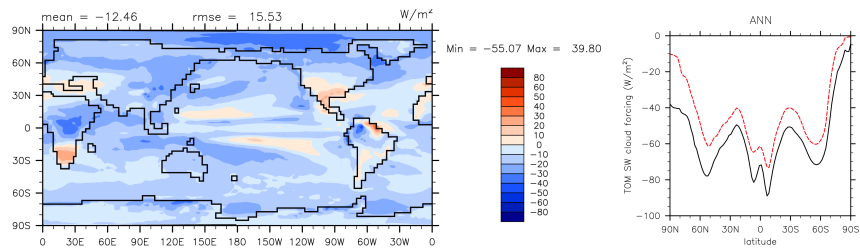
To oppose the longwave cloud forcing, shortwave cloud forcing decreases in the modified Miocene simulations (Figure 6.29). In the 400 ppm CO<sub>2</sub> modified case when compared to the control, there is an average decrease of 15.47 W/m<sup>2</sup>. Shortwave cloud forcing decreases in for modified simulations across the entire globe. Although there is notable increases shown in the Southern tip of Africa and the Northeast corner of South America for the 800 ppm CO<sub>2</sub> simulation.

## Shortwave Cloud Forcing Difference

(a) Miocene 400 simulation (modified - control at 400)



(b) Miocene 800 simulation (modified - control at 400)



(c) Miocene 800 - Miocene 400 simulation

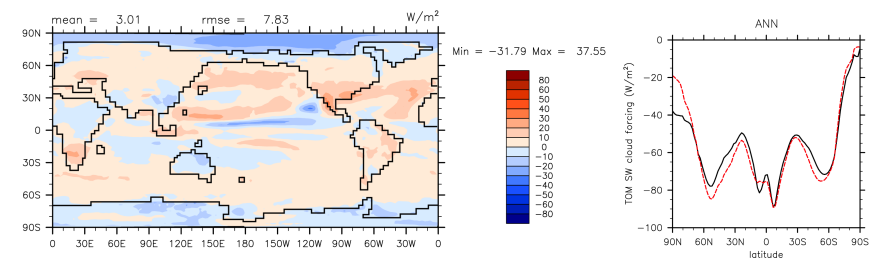


Figure 6.29.: Shortwave cloud forcing difference plot for the modified SLF simulations are shown on the left. The zonal mean plot for SLF simulations (black) and reference simulations (red dashed) are on the right.

## 7 DISCUSSION

The hypothesis seeks to answer the question, "are general circulation models missing key cloud processes or feedbacks that can capture the mid-Miocene warmth?" The pre-industrial and modern cases give insight to what and how the modifications change the overall climate trends represented in the climate models.

### 7.1 Temperature

First and foremost, the modifications in every simulation when compared to its control have an increase in average global surface temperature, as expected. The model sensitivity to  $\text{CO}_2$  is also captured, with higher ppm values enhancing the warming more than lower ppm values. The warming mainly occurred over the arctic regions. At 800 ppm  $\text{CO}_2$ , the entire globe warms, while lower values show a cooling pocket over the eastern Pacific Ocean. Therefore there is a weaker equator-to-pole temperature gradient in the modified simulations. Both the slab ocean cases and Miocene simulation's vertical contour plots have the same signature across altitude and latitude for temperature.

Across the Miocene simulations, similar results are seen. The land masses also had significant warming in areas such as Africa and South America. Those two continents are the first to warm as levels of  $\text{CO}_2$  increase across the slab ocean simulations. The Miocene 400 simulation shows the weakening of the equator to pole temperature gradient, which is a key characteristic of past greenhouse climates. Another key feature of greenhouse climates are the enhanced average surface temperature. Again, the Miocene simulations with modifications also capture this feature that other greenhouse climates possess. Since changes were made to the model's cloud properties,

we must look at how the clouds represented in the model changed to get a better understanding of how the arctic and overall warming was generated.

## 7.2 Cloud Amount

As expected, there is an overall increase in cloud amount as shown in the model across the entire planet for the modified cases. The largest increase in cloud amount is mainly at high altitudes and the increase in high clouds is maximized at higher latitudes. The vertical contour plots for total cloud amount in Figure 6.11 sums this finding up nicely. Upper-level clouds are increasing over the northern mid to high latitudes for the slab ocean cases. In the Miocene, there are significant areas of increase in high clouds over Africa and South America that align with the locations of increase in surface temperature. The modifications made to the simulations were specifically designed to increase cloud fraction and in particular the super cooled liquid fraction which affects high altitude ice clouds. However, it is important to note that there is an increase in mid-level cloud amounts in the pre-industrial case, but at higher values of  $p\text{CO}_2$  the mid-level clouds show little change between the controlled and modified simulations. Therefore, increase in cloud fraction plays a role in the enhanced warming over the poles as the maximum increase in cloud fraction is over the polar regions in both hemispheres. The cloud forcing can explain the enhanced warming feedback.

## Cloud Radiative Effect

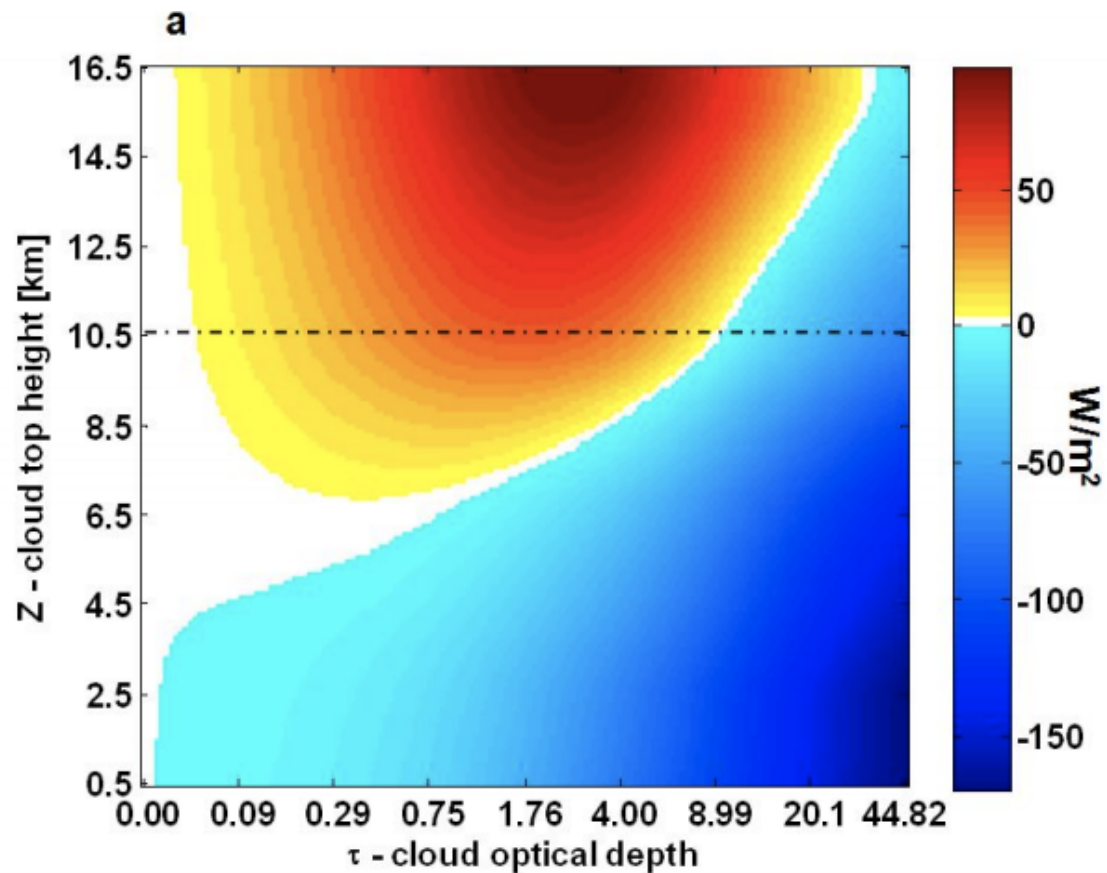


Figure 7.1.: Cloud radiative forcing is represented in the  $\tau$  (cloud optical depth) and  $Z$  (cloud top altitude) space. Contours are showing  $W/m^2$  at the top of the atmosphere for daily averages. Figure is from Koren et al. 2010.

### 7.3 Forcing and Fluxes

As upper-level cloud amount increase, a warming trend is observed in response as high level clouds which are expected to provide overall warming by absorbing Earth's outgoing thermal radiation. The longwave cloud forcing results provide evidence that the model's enhanced warming are coming from the high level clouds.

## Forcing and Fluxes Summary

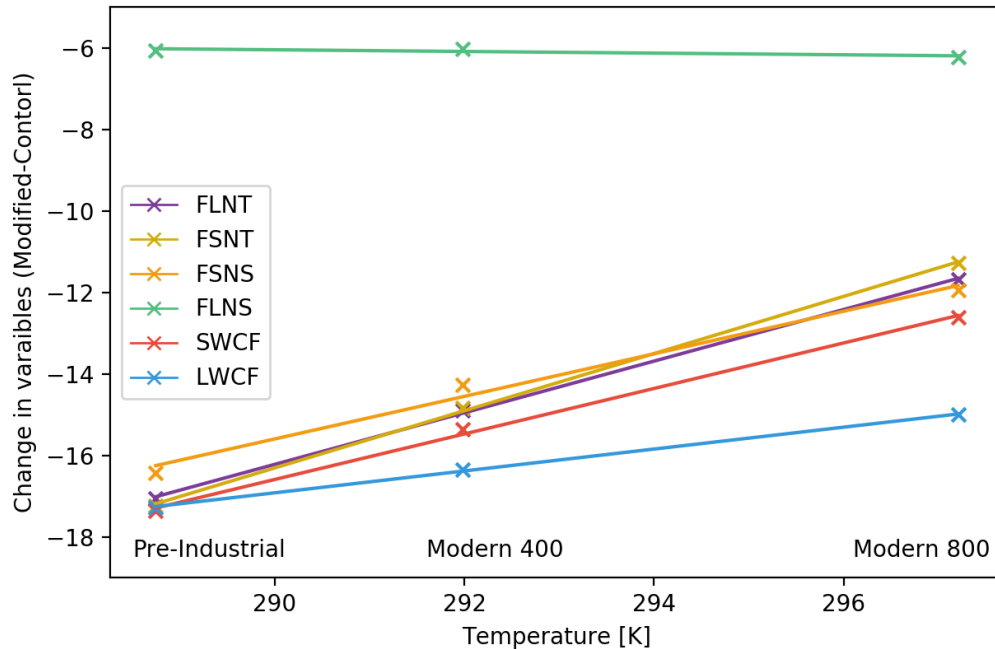


Figure 7.2.: Trend lines of differences of the modified simulations by their control for top of model net longwave flux (FLNT), top of model net shortwave flux (FSNT), surface net longwave flux (FLNS), surface net shortwave flux (FSNS), longwave cloud forcing (LWCF), and shortwave cloud forcing (SWCF) plotted against the temperature for modified simulations (pre-industrial, modern 400 CO<sub>2</sub>, and modern 800 CO<sub>2</sub>).

The warming trend from upper-level clouds agrees with findings from Koren et al. 2010 shown in Figure 7.1 [122]. Koren et al. 2010 shows that thick high clouds have a net warming effect (positive radiative forcing), represented in the warm color contours, and low-level clouds have a net cooling effect (negative radiative forcing) represented in cool colors.

The upper-level cloud response is seen across all cases, pre-industrial, modern, and Miocene, yet there is also an increase in low level clouds more notably across the simulations with lower CO<sub>2</sub>. Lower level clouds were not expected to change drastically in the modifications and need to be analyzed further. These low level

clouds decrease the shortwave cloud forcing across all modified versions of the model. This effect works to cool the model by reflecting incoming shortwave solar radiation.

There is a definite decrease in shortwave cloud forcing across all simulations when compared to their respective control cases. Below, Table 7.1 shows the average decrease and increase for the four simulation differences from modified to control cases of the shortwave cloud forcing and longwave cloud forcing, respectively. As CO<sub>2</sub> values increase, moving down the table, there is greater difference between shortwave and longwave cloud forcing, corresponding to temperature feedbacks in the models. Shortwave cloud forcing weakens at higher values of CO<sub>2</sub> when modifications are made to the model. Therefore, long wave cloud forcing is shown to dominate more than the shortwave cloud forcing to produce an enhanced net warming effect. A summary of the forcing and fluxes are shown in Figure 7.2.

A difference of 1 W/m<sup>2</sup> between the shortwave cloud forcing and the longwave cloud forcing is equivalent to about 1°C of warming. Referencing Table 7.1, the pre-industrial case shows little to no warming, the modern cases show a range of a 0.5°C to about 1°C warming, and doubling CO<sub>2</sub> to 800 ppm shows over 2°C of warming between the control and modified. These approximations are verified by the temperature difference from control to modified found in all of the simulations.

Table 7.1.: Table of values for the average shortwave cloud forcing (SWCF) and longwave cloud forcing (LWCF) difference between modified cases and control cases.

Cloud Forcing Differences: Modified - Control			
Case	SWCF	LWCF	Difference
PI	-17.30	17.28	-0.02
Modern	-15.07	16.22	1.15
Modern 400	-15.90	16.35	0.45
Modern 800	-12.41	14.88	2.47

## 8 CONCLUSION

Changes to cloud microphysical properties were made to the Community Atmospheric Model and implemented in twelve general circulation model simulations to test the hypothesis that cloud microphysical property-aerosol feedbacks explain the Miocene warmth at near-modern concentrations of CO<sub>2</sub>, approximately 400 ppm. The simulations analyzed ranged from the mid-Miocene to modern day cases and ran at varying CO<sub>2</sub> from 284.7 to 800 ppm. The modifications made use of an aerosol dependent ice nucleation mechanism versus the default temperature and supersaturation based ice nucleation parameterization previously used in CAM5. Another key modification found in this study is implementing a theory based cloud phase separation instead of an observation based phase separation algorithm, previously used in CAM5.

The slab ocean cases all had enhanced warming over the high latitudes, overall greater mean annual surface temperature than the control cases, and increase in high clouds across the planet. It is found that dominance in the longwave cloud forcing over the shortwave cloud forcing led to an increase in warming and was amplified as CO<sub>2</sub> levels increased. Based on these results, current climate models could be underestimating how warm our planet will get as CO<sub>2</sub> increases and climate change progresses.

Results showed that significant warming was represented in the modified cases and was seen to be amplified with increasing CO<sub>2</sub>. This warming mainly occurs over the arctic regions and over the landmasses in the Miocene, which provides a weaker equator to pole temperature gradient. The enhanced warming over the poles correlate to the characteristics of past greenhouse climates. This warming was found to be a response to the increase in upper-level cloud fraction from the modifications made to the model. The high clouds absorb longwave radiation and warm the globe. The location of high cloud increase correspond to the locations of maximum warming. It

was found that the longwave cloud forcing thus dominates over the shortwave cloud forcing for a net warming effect. Yet the modifications also produced an unexpected decrease in shortwave cloud forcing as well, thus acting to cool the planet. This effect will need to be explored more in depth in future studies, but note it could pertain to the slight increase in lower level clouds.

Other future work can be done to explore the greenhouse climate characteristic of reduced inner continental seasonality. The circulation trends, El Nino Southern Oscillations, and comparisons against observational data are other areas to be further explored using the global climate model data collected from the modified simulations in this study.

## REFERENCES

- [1] Matthew Huber. Progress in greenhouse climate modeling. *The Paleontological Society Papers*, 18:50, 2012.
- [2] Madelaine Bohme, Angela A. Bruch, and Alfred Selmeier. The reconstruction of early and middle miocene climate and vegetation in southern germany as determined from the fossil wood flora. *Palaeogeography, Palaeoclimatology, Palaeoecology*, 253(1):91–114, 2007.
- [3] Matthew J. Pound, Alan M. Haywood, Ulrich Salzmann, and James B. Riding. Global vegetation dynamics and latitudinal temperature gradients during the mid to late miocene (15.975–33ma). *Earth-Science Reviews*, 112:1–22, 2012.
- [4] J.C. Zachos, Gerald Dickens, and Richard E Zeebe. An early cenozoic perspective on greenhouse warming and carbon cycle dynamics. *Nature*, 451:279–83, 2008.
- [5] Amelia E. Shevenell, James P. Kennett, and David W. Lea. Middle miocene ice sheet dynamics, deep-sea temperatures, and carbon cycling: A southern ocean perspective. *Geochemistry, Geophysics, Geosystems*, 9(2), 2008.
- [6] A.-J. Henrot, T. Utescher, B. Erdei, M. Dury, N. Hamon, G. Ramstein, M. Krapp, N. Herold, A. Goldner, E. Favre, G. Munhoven, and L. Franois. Middle miocene climate and vegetation models and their validation with proxy data. *Palaeogeography, Palaeoclimatology, Palaeoecology*, 467:95–119, 2017.
- [7] M. P. S. Badger, D. N. Schmidt, A. Mackensen, and R. D. Pancost. High-resolution alkenone palaeobarometry indicates relatively stable pCO<sub>2</sub> during the pliocene (3.3–2.8 ma). *Philosophical Transactions of the Royal Society A: Mathematical, Physical and Engineering Sciences*, 371(2001):20130094–20130094, 2013.
- [8] David J. Beerling and Dana L. Royer. Convergent cenozoic CO<sub>2</sub> history. *Nature Geoscience*, 4:418, 2011.
- [9] Gavin L. Foster, Caroline H. Lear, and James W.B. Rae. The evolution of pCO<sub>2</sub>, ice volume and climate during the middle miocene. *Earth and Planetary Science Letters*, 341–344:243–254, 2012.
- [10] Zhang Yi Ge, Pagani Mark, Liu Zhonghui, Bohaty Steven M., and DeConto Robert. A 40-million-year history of atmospheric CO<sub>2</sub>. *Philosophical Transactions of the Royal Society A: Mathematical, Physical and Engineering Sciences*, 371(2001):20130096, 2013.
- [11] Xiuquan Wan, Ping Chang, R. Saravanan, Rong Zhang, and Matthew W. Schmidt. On the interpretation of caribbean paleo-temperature reconstructions during the younger dryas. *Geophysical Research Letters*, 36(2), 2009.

- [12] P.J. Markwick. The palaeogeographic and palaeoclimatic significance of climate proxies for data-model comparisons. In M. Williams, A.M. Haywood, F.J. Gregory, and D.N. Schmidt, editors, *Deep-Time Perspectives on Climate Change: Marrying the Signal from Computer Models and Biological Proxies*, pages 251–312. The Geological Society of London on behalf of The Micropalaeontological Society, first edition, 2007.
- [13] Tammo Reichgelt, Elizabeth M. Kennedy, Dallas C. Mildenhall, John G. Conran, David R. Greenwood, and Daphne E. Lee. Quantitative palaeoclimate estimates for early miocene southern new zealand: Evidence from foulden maar. *Palaeogeography, Palaeoclimatology, Palaeoecology*, 378:36–44, 2013.
- [14] Torsten Utescher, Angela A. Bruch, Arne Micheels, Volker Mosbrugger, and Svetlana Popova. Cenozoic climate gradients in eurasia a palaeo-perspective on future climate change? *Palaeogeography, Palaeoclimatology, Palaeoecology*, 304(3):351–358, 2011.
- [15] A. Goldner, N. Herold, and M. Huber. The challenge of simulating the warmth of the mid-miocene climatic optimum in CESM1. *Climate of the Past*, 10(2):523–536, 2014.
- [16] C. H. Lear. Cenozoic deep-sea temperatures and global ice volumes from mg/ca in benthic foraminiferal calcite. *Science*, 287(5451):269–272, 2000.
- [17] Y. You, M. Huber, R. D. Mller, C. J. Poulsen, and J. Ribbe. Simulation of the middle miocene climate optimum. *Geophysical Research Letters*, 36(4), 2009.
- [18] Rongzhi Zhang, Florent Murat, Caroline Pont, Thierry Langin, and Jerome Salse. Paleo-evolutionary plasticity of plant disease resistance genes. *BMC Genomics*, 15(1):187, 2014.
- [19] Mark Pagani, James C. Zachos, Katherine H. Freeman, Brett Tipple, and Stephen Bohaty. Marked decline in atmospheric carbon dioxide concentrations during the paleogene. *Science (New York, N.Y.)*, 309(5734):600–603, 2005.
- [20] Paul Pearson and Martin Palmer. Pearson, p. n. & palmer, m. r. atmospheric carbon dioxide over the past 60 million years. *Nature*, 406:695–9, 2000.
- [21] Wolfram M. Krschner, Zlatko Kvaek, and David L. Dilcher. The impact of miocene atmospheric carbon dioxide fluctuations on climate and the evolution of terrestrial ecosystems. *Proceedings of the National Academy of Sciences*, 105(2):449–453, 2008.
- [22] A.-J. Henrot, L. Franois, E. Favre, M. Butzin, M. Ouberdous, and G. Munhoven. Effects of CO<sub>2</sub>, continental distribution, topography and vegetation changes on the climate at the middle miocene: A model study. *Climate of the Past*, 6(5):675–694, 2010.
- [23] J.A. Tong, Yonglim You, Dietmar Mller, and Maria Seton. Climate model sensitivity to atmospheric CO<sub>2</sub> concentrations for the middle miocene. *Global and Planetary Change*, 67:129–140, 2009.
- [24] N. Herold, M. Huber, and R. D. Mller. Modeling the miocene climatic optimum. part i: Land and atmosphere. *Journal of Climate*, 24(24):6353–6372, 2011.

- [25] M. Krapp and J. H. JungCLAUS. The middle miocene climate as modelled in an atmosphere-ocean-biosphere model. *Climate of the Past*, 7(4):1169–1188, 2011.
- [26] Timothy D. Herbert and Jeffrey D. Schuffert. ALKENONE UNSATURATION ESTIMATES OF SEA-SURFACE TEMPER. *Proceedings of the Ocean Drilling Program, Scientific Results*, 159T, 1998.
- [27] Jeremy R. Marlow, Carina B. Lange, Gerold Wefer, and Antoni Rosell-Mel. Upwelling intensification as part of the pliocene-pleistocene climate transition. *Science*, 290(5500):2288–2291, 2000.
- [28] Petra S. Dekens, Ana Christina Ravelo, and Matthew D. McCarthy. Warm upwelling regions in the pliocene warm period. *Paleoceanography*, 22(3), 2007.
- [29] Gaojun Li, Thomas Pettke, and Jun Chen. Increasing  $\delta^{18}O$  isotopic ratio of asian dust indicates progressive uplift of the north tibetan plateau since the middle miocene. *Geology*, 39(3):199–202, 2011.
- [30] Jeroen Groeneveld, Silke Steph, Ralf Tiedemann, C.-Dieter Garbe-Schnberg, Dirk Nrnberg, and Arne Sturm. Pliocene mixed-layer oceanography for site 1241, using combined mg/ca and  $\delta^{18}O$  analyses of globigerinoides sacculifer. In *Proceedings of the Ocean Drilling Program, Scientific Results*, volume 202, 2006.
- [31] Matthew Huber and Rodrigo Caballero. Eocene el nio: Evidence for robust tropical dynamics in the "hothouse". *Science*, 299(5608):877–881, 2003.
- [32] Dowsett Harry J and Robinson Marci M. Mid-pliocene equatorial pacific sea surface temperature reconstruction: a multi-proxy perspective. *Philosophical Transactions of the Royal Society A: Mathematical, Physical and Engineering Sciences*, 367(1886):109–125, 2009.
- [33] Bonham Sarah G, Haywood Alan M, Lunt Daniel J, Collins Mathew, and Salzmann Ulrich. El niosouthern oscillation, pliocene climate and equifinality. *Philosophical Transactions of the Royal Society A: Mathematical, Physical and Engineering Sciences*, 367(1886):127–156, 2009.
- [34] R. E. M. Rickaby and P. Halloran. Cool la nia during the warmth of the pliocene? *Science*, 307(5717):1948–1952, 2005.
- [35] Carl Wunsch. A perpetually running ENSO in the pliocene? *Journal of Climate*, 22(12):3506–3510, 2009.
- [36] Simone Galeotti, Srinath Krishnan, Mark Pagani, Luca Lanci, Alberto Gaudio, James C. Zachos, Simonetta Monechi, Guia Morelli, and Lucas Lourens. Orbital chronology of early eocene hyperthermals from the contessa road section, central italy. *Earth and Planetary Science Letters*, 290(1):192–200, 2010.
- [37] N. Scroxtton, S. G. Bonham, R. E. M. Rickaby, S. H. F. Lawrence, M. Hermoso, and A. M. Haywood. Persistent el niosouthern oscillation variation during the pliocene epoch. *Paleoceanography*, 26(2), 2011.
- [38] A. V. Fedorov, R. C. Pacanowski, S. G. Philander, and G. Boccaletti. The effect of salinity on the wind-driven circulation and the thermal structure of the upper ocean. *Journal of Physical Oceanography*, 34(9):1949–1966, 2006.

- [39] A. V. Fedorov. The pliocene paradox (mechanisms for a permanent el nino). *Science*, 312(5779):1485–1489, 2006.
- [40] Gerald H. Haug and Ralf Tiedemann. Effect of the formation of the isthmus of panama on atlantic ocean thermohaline circulation. *Nature*, 393(6686):673, 1998.
- [41] Ralph Klcker, Gerald M. Ganssen, Simon J. A. Jung, Dick Kroon, and Rüdiger Henrich. *Age, pteropoda counts and Limacina dissolution index of sediment core NIOP-C25-905-BC*. PANGAEA, 2005.
- [42] Silke Steph, Ralf Tiedemann, Matthias Prange, Jeroen Groeneveld, Michael Schulz, Axel Timmermann, Dirk Nürnberg, Carsten Röhlemann, Cornelia Saukel, and Gerald H. Haug. Early pliocene increase in thermohaline overturning: A precondition for the development of the modern equatorial pacific cold tongue.
- [43] Katherine E. Dayem, Peter Molnar, Marin K. Clark, and Gregory A. Houseman. Far-field lithospheric deformation in tibet during continental collision. *Tectonics*, 28(6), 2009.
- [44] Peter Molnar and Mark A. Cane. Early pliocene (preice age) el niolike global climate: Which el nio? *Geosphere*, 3(5):337–365, 2007.
- [45] N. Herold, M. Huber, R. D. Müller, and M. Seton. Modeling the miocene climatic optimum: Ocean circulation: MODELING MIOCENE OCEAN CIRCULATION. *Paleoceanography*, 27, 2012.
- [46] A. V. Fedorov, C. M. Brierley, K. T. Lawrence, Z. Liu, P. S. Dekens, and A. C. Ravelo. Patterns and mechanisms of early pliocene warmth. *Nature*, 496:43, 2013.
- [47] Ruediger Stein, Kirsten Fahl, Michael Schreck, Gregor Knorr, Frank Niessen, Matthias Forwick, Catalina Gebhardt, Laura Jensen, Michael Kaminski, Achim Kopf, Jens Matthiessen, Wilfried Jokat, and Gerrit Lohmann. Evidence for ice-free summers in the late miocene central arctic ocean. *Nature Communications*, 7:11148, 2016.
- [48] Ann Holbourn, Wolfgang Kuhnt, Michael Schulz, and Helmut Erlenkeuser. Impacts of orbital forcing and atmospheric carbon dioxide on miocene ice-sheet expansion. *Nature*, 438(7067):483–487, 2005.
- [49] Mitchell Lyle, John Barron, Timothy J. Bralower, Matthew Huber, Annette Olivarez Lyle, A. Christina Ravelo, David K. Rea, and Paul A. Wilson. Pacific ocean and cenozoic evolution of climate. *Reviews of Geophysics*, 46(2), 2008.
- [50] Daniel J. Lunt, Rachel Flecker, Paul J. Valdes, Ulrich Salzmann, Rupert Gladstone, and Alan M. Haywood. A methodology for targeting palaeo proxy data acquisition: A case study for the terrestrial late miocene. *Earth and Planetary Science Letters*, 271(1):53–62, 2008.
- [51] Matthew Huber. A sensitivity to history. *Nature Geoscience*, 6:15–16, 2013.
- [52] IPCC. *Summary for Policymakers*, book section SPM, page 130. Cambridge University Press, Cambridge, United Kingdom and New York, NY, USA, 2013.

- [53] David M. Winker, Mark A. Vaughan, Ali Omar, Yongxiang Hu, Kathleen A. Powell, Zhaoyan Liu, William H. Hunt, and Stuart A. Young. Overview of the CALIPSO mission and CALIOP data processing algorithms. *Journal of Atmospheric and Oceanic Technology*, 26(11):2310–2323, 2009.
- [54] Ivy Tan and Trude Storelvmo. Sensitivity study on the influence of cloud microphysical parameters on mixed-phase cloud thermodynamic phase partitioning in CAM5. *Journal of the Atmospheric Sciences*, 73(2):709–728, 2016.
- [55] O. Boucher, D. Randall, P. Artaxo, C. Bretherton, G. Feingold, P. Forster, V.-M. Kerminen, Y. Kondo, H. Liao, U. Lohmann, P. Rasch, S. K. Satheesh, S. Sherwood, B. Stevens, and X. Y. Zhang. *Clouds and aerosols*, pages 571–657. Cambridge University Press, Cambridge, UK, 2013.
- [56] Norman McFarlane. Parameterizations: Representing key processes in climate models without resolving them. *Wiley Interdisciplinary Reviews: Climate Change*, 2, 07 2011.
- [57] Muge Komurcu, Trude Storelvmo, Ivy Tan, Ulrike Lohmann, Yuxing Yun, Joyce E. Penner, Yong Wang, Xiaohong Liu, and Toshihiko Takemura. Intercomparison of the cloud water phase among global climate models: CLOUD WATER PHASE IN GCMs. *Journal of Geophysical Research: Atmospheres*, 119(6):3372–3400, 2014.
- [58] I. Tan, T. Storelvmo, and M. D. Zelinka. Observational constraints on mixed-phase clouds imply higher climate sensitivity. *Science*, 352(6282):224–227, 2016.
- [59] Richard B Neale, Jadwiga H Richter, Andrew J Conley, Sungsu Park, Peter H Lauritzen, Andrew Gettelman, David L Williamson, Philip J Rasch, Stephen J Vavrus, Mark A Taylor, William D Collins, Minghua Zhang, and Shian-Jiann Lin. Description of the NCAR community atmosphere model (CAM 4.0). *NCAR Technical Notes*, page 224, 2010.
- [60] G. J. Zhang and N. A. McFarlane. Sensitivity of climate simulations to the parameterization of cumulus convection in the canadian climate centre general circulation model. *Atmosphere-Ocean*, 33(3):407–446, Sep 1995.
- [61] Jadwiga H. Richter and Philip J. Rasch. Effects of convective momentum transport on the atmospheric circulation in the community atmosphere model, version 3. *Journal of Climate*, 21(7):1487–1499, 2008.
- [62] David J. Raymond and Alan M. Blyth. A stochastic mixing model for nonprecipitating cumulus clouds. *Journal of the Atmospheric Sciences*, 43(22):2708–2718, 1986.
- [63] David J. Raymond and Alan M. Blyth. Extension of the stochastic mixing model to cumulonimbus clouds. *Journal of the Atmospheric Sciences*, 49(21):1968–1983, 1992.
- [64] Steve Vavrus and Duane Waliser. An improved parameterization for simulating arctic cloud amount in the CCSM3 climate model. *Journal of Climate*, 21(21):5673–5687, 2008.

- [65] Minghua Zhang, Wuyin Lin, Christopher S. Bretherton, James J. Hack, and Phillip J. Rasch. A modified formulation of fractional stratiform condensation rate in the NCAR community atmospheric model (CAM2). *Journal of Geophysical Research*, 2003.
- [66] P. J. Rasch and J. E. Kristjansson. A comparison of the CCM3 model climate using diagnosed and predicted condensate parameterizations. *Journal of Climate*, 11(7):1587–1614, 1998.
- [67] William D. Collins. Parameterization of generalized cloud overlap for radiative calculations in general circulation models. *Journal of the Atmospheric Sciences*, 58(21):3224–3242, 2001.
- [68] Richard B Neale, Andrew Gettelman, Sungsu Park, Chih-Chieh Chen, Peter H Lauritzen, David L Williamson, Andrew J Conley, Doug Kinnison, Dan Marsh, Anne K Smith, Francis Vitt, Rolando Garcia, Jean-Francois Lamarque, Mike Mills, Simone Tilmes, Hugh Morrison, Philip Cameron-Smith, William D Collins, Michael J Iacono, Richard C Easter, Xiaohong Liu, Steven J Ghan, Philip J Rasch, and Mark A Taylor. Description of the NCAR community atmosphere model (CAM 5.0). *NCAR Technical Notes*, page 289, 2012.
- [69] Christopher S. Bretherton and Sungsu Park. A new moist turbulence parameterization in the community atmosphere model. *Journal of Climate*, 22:3422–3448, 2009.
- [70] Hugh Morrison and Andrew Gettelman. A new two-moment bulk stratiform cloud microphysics scheme in the community atmosphere model, version 3 (CAM3). part i: Description and numerical tests. *Journal of Climate*, 21(15):3642–3659, 2008.
- [71] Xiaohong Liu, Joyce E. Penner, Steven J. Ghan, and Minghuai Wang. Inclusion of ice microphysics in the NCAR community atmospheric model version 3 (CAM3). *Journal of Climate*, 20(18):4526–4547, 2007.
- [72] A. Gettelman, X. Liu, S. J. Ghan, H. Morrison, S. Park, A. J. Conley, S. A. Klein, J. Boyle, D. L. Mitchell, and J.-L. F. Li. Global simulations of ice nucleation and ice supersaturation with an improved cloud scheme in the community atmosphere model. *Journal of Geophysical Research: Atmospheres*, 115, 2010.
- [73] S. Park, C. S. Bretheron, and P. J. Rasch. The revised cloud macrophysics in the community atmosphere model. *Journal of Climate*, 2010.
- [74] X. Liu and S. Ghan. A modal aerosol model implementation in the community atmosphere model, version 5 (cam5). *Journal of Atmospheric Science*, 2010.
- [75] J.-F. Lamarque, T. C. Bond, V. Eyring, C. Granier, A. Heil, Z. Klimont, D. Lee, C. Liou, A. Mieville, B. Owen, M. G. Schultz, D. Shindell, S. J. Smith, E. Stehfest, J. Van Aardenne, O. R. Cooper, M. Kainuma, N. Mahowald, J. R. McConnell, V. Naik, K. Riahi, and D. P. van Vuuren. Historical (1850-2000) gridded anthropogenic and biomass burning emissions of reactive gases and aerosols: methodology and application. *Atmospheric Chemistry and Physics*, 10(15):7017–7039, 2010.

- [76] Tami C. Bond, Ekta Bhardwaj, Rong Dong, Rahil Jogani, Soonkyu Jung, Christoph Roden, David G. Streets, and Nina M. Trautmann. Historical emissions of black and organic carbon aerosol from energy-related combustion, 1850-2000. *Global Biogeochemical Cycles*, 21(2), 6 2007.
- [77] C Junker and C Liousse. A global emission inventory of carbonaceous aerosol from historic records of fossil fuel and biofuel consumption for the period 1860–1997. *Atmos. Chem. Phys.*, page 13, 2008.
- [78] Steven J Smith, Hugh Pitcher, and T. M. L Wigley. Global and regional anthropogenic sulfur dioxide emissions. *Global and Planetary Change*, 29(1):99–119, 2001.
- [79] Steven J. Smith, Robert Andres, Elvira Conception, and Joshua Lurz. Historical sulfur dioxide emissions 1850-2000: Methods and results. *Pacific Northwest National Laboratory*, (PNNL-14537, 15020102), 2004.
- [80] Steven J. Ghan and Rahul A. Zaveri. Parameterization of optical properties for hydrated internally mixed aerosol. *Journal of Geophysical Research: Atmospheres*, 112(D10), 5 2007.
- [81] J. Wiscombe. Mie scattering calculations: Advances in technique and fast, vector-speed computer codes. *NCAR Technical Notes*, 1979.
- [82] David L. Mitchell. Effective diameter in radiation transfer: General definition, applications, and limitations. *Journal of the Atmospheric Sciences*, 59(15):2330–2346, 2002.
- [83] Michael J. Iacono, Jennifer S. Delamere, Eli J. Mlawer, Mark W. Shephard, Shepard A. Clough, and William D. Collins. Radiative forcing by long-lived greenhouse gases: Calculations with the aer radiative transfer models. *Journal of Geophysical Research: Atmospheres (1984-2012)*, 113(D13), 7 2008.
- [84] Eli J. Mlawer, Steven J. Taubman, Patrick D. Brown, Michael J. Iacono, and Shepard A. Clough. Radiative transfer for inhomogeneous atmospheres: RRTM, a validated correlated-k model for the longwave. *Journal of Geophysical Research: Atmospheres*, 102(D14):16663–16682, 7 1997.
- [85] Y.-M. Wang, J. L. Lean, and Jr N. R. Sheeley. Modeling the sun's magnetic field and irradiance since 1713. *The Astrophysical Journal*, 625(1):522, 2005.
- [86] Robert Pincus, Howard W. Barker, and Jean-Jacques Morcrette. A fast, flexible, approximate technique for computing radiative transfer in inhomogeneous cloud fields. *Journal of Geophysical Research: Atmospheres (1984-2012)*, 108(D13), 7 2003.
- [87] G. Cesana, D. E. Waliser, X. Jiang, and J.-L. F. Li. Multimodel evaluation of cloud phase transition using satellite and reanalysis data. *Journal of Geophysical Research: Atmospheres*, 120(15):7871–7892, 2015.
- [88] Zamin A. Kanji, Luis A. Ladino, Heike Wex, Yvonne Boose, Monika Burkert-Kohn, Daniel J. Cziczo, and Martina Krmer. Overview of ice nucleating particles. *Meteorological Monographs*, 58:1.1–1.33, 2017.

- [89] P. J. DeMott, A. J. Prenni, G. R. McMeeking, R. C. Sullivan, M. D. Petters, Y. Tobo, M. Niemand, O. Mhler, J. R. Snider, Z. Wang, and S. M. Kreidenweis. Integrating laboratory and field data to quantify the immersion freezing ice nucleation activity of mineral dust particles. *Atmospheric Chemistry and Physics*, 15(1):393–409, 2015.
- [90] P. J. DeMott, A. J. Prenni, X. Liu, S. M. Kreidenweis, M. D. Petters, C. H. Twohy, M. S. Richardson, T. Eidhammer, and D. C. Rogers. Predicting global atmospheric ice nuclei distributions and their impacts on climate. *Proceedings of the National Academy of Sciences*, 107(25):11217–11222, 2010.
- [91] J. Fan, L. R. Leung, P. J. DeMott, J. M. Comstock, B. Singh, D. Rosenfeld, J. M. Tomlinson, A. White, K. A. Prather, P. Minnis, J. K. Ayers, and Q. Min. Aerosol impacts on california winter clouds and precipitation during CalWater 2011: local pollution versus long-range transported dust. *Atmospheric Chemistry and Physics*, 14(1):81–101, 2014.
- [92] Benjamin S. Grandey, Daniel Rothenberg, Alexander Avramov, Qinjian Jin, Hsiang-He Lee, Xiaohong Liu, Zheng Lu, Samuel Albani, and Chien Wang. Effective radiative forcing in the aerosol-climate model CAM5.3-MARC-ARG. *Atmospheric Chemistry and Physics*, 18(21):15783–15810, 2018.
- [93] Kenneth Sassen. The polarization lidar technique for cloud research: A review and current assessment. *Bulletin of the American Meteorological Society*, 72(12):1848–1866, 1991.
- [94] Yongxiang Hu, David Winker, Mark Vaughan, Bing Lin, Ali Omar, Charles Trepte, and David Flittner. CALIPSO/CALIOP cloud phase discrimination algorithm.
- [95] Ali H. Omar, David M. Winker, Mark A. Vaughan, Yongxiang Hu, Richard A. Trepte, Charles R. and Ferrare, Kam-Pui Lee, and Chris A. Hostetler. The CALIPSO automated aerosol classification and lidar ratio selection algorithm, 2009.
- [96] Volker Mosbrugger, Torsten Utescher, and David L. Dilcher. Cenozoic continental climatic evolution of central europe. *Proceedings of the National Academy of Sciences*, 102(42):14964–14969, 2005.
- [97] Angela A. Bruch, Dieter Uhl, and Volker Mosbrugger. Miocene climate in europe patterns and evolution: A first synthesis of NECLIME. *Palaeogeography, Palaeoclimatology, Palaeoecology*, 253(1):1–7, 2007.
- [98] Angela A. Bruch, Torsten Utescher, and Volker Mosbrugger. Precipitation patterns in the miocene of central europe and the development of continentality. *Palaeogeography, Palaeoclimatology, Palaeoecology*, 304(3):202–211, 2011.
- [99] Jonathan P. LaRiviere, A. Christina Ravelo, Allison Crimmins, Petra S. Dekens, Heather L. Ford, Mitch Lyle, and Michael W. Wara. Late miocene decoupling of oceanic warmth and atmospheric carbon dioxide forcing. *Nature*, 486(7401):97–100, 2012.
- [100] N. Herold, M. Seton, R. D. Mller, Y. You, and M. Huber. Middle miocene tectonic boundary conditions for use in climate models: MIDDLE MIOCENE TECTONIC BOUNDARY CONDITIONS. *Geochemistry, Geophysics, Geosystems*, 9(10), 2008.

- [101] Adrianj Hartley. Andean uplift and climate change. *Journal of the Geological Society*, 160(1):7–10, 2003.
- [102] C. Hoorn, F. P. Wesselingh, H. ter Steege, M. A. Bermudez, A. Mora, J. Sevink, I. Sanmartn, A. Sanchez-Meseguer, C. L. Anderson, J. P. Figueiredo, C. Jaramillo, D. Riff, F. R. Negri, H. Hooghiemstra, J. Lundberg, T. Stadler, T. Srkinen, and A. Antonelli. Amazonia through time: Andean uplift, climate change, landscape evolution, and biodiversity. *Science*, 330(6006):927–931, 2010.
- [103] G. E. Shephard, R. D. Mller, L. Liu, and M. Gurnis. Miocene drainage reversal of the amazon river driven by platemantle interaction. *Nature Geoscience*, 3(12):870–875, 2010.
- [104] Manuel Iturralde-Vinent. Meso-cenozoic caribbean paleogeography: Implications for the historical biogeography of the region. *International Geology Review - INT GEOL REV*, 48:791–827, 2006.
- [105] B. S. Cramer, K. G. Miller, P. J. Barrett, and J. D. Wright. Late cretaceous-neogene trends in deep ocean temperature and continental ice volume: Reconciling records of benthic foraminiferal geochemistry (18o and mg/ca) with sea level history. *Journal of Geophysical Research: Oceans*, 116, 2011.
- [106] S Pekar and Robert M. DeConto. High-resolution ice-volume estimates for the early miocene: evidence for a dynamic ice sheet in antarctica. *Palaeogeography, Palaeoclimatology, Palaeoecology*, 231:101–109, 2006.
- [107] J. Zachos, Mark Pagani, Lisa Sloan, Ellen Thomas, and Katharina Billups. Trends, rhythms, and aberrations in global climate 65 ma to present. *Science*, 292(5517):686–693, 2001.
- [108] David Pollard and Robert M. DeConto. Modelling west antarctic ice sheet growth and collapse through the past five million years. *Nature*, 458(7236):329–332, 2009.
- [109] Douglas S. Wilson and Bruce P. Luyendyk. West antarctic paleotopography estimated at the eocene-oligocene climate transition. *Geophysical Research Letters*, 36(16), 2009.
- [110] P. Fretwell, H. D. Pritchard, D. G. Vaughan, J. L. Bamber, N. E. Barrand, R. Bell, C. Bianchi, R. G. Bingham, D. D. Blankenship, G. Casassa, G. Catania, D. Callens, H. Conway, A. J. Cook, H. F. J. Corr, D. Damaske, V. Damm, F. Ferraccioli, R. Forsberg, S. Fujita, Y. Gim, P. Gogineni, J. A. Griggs, R. C. A. Hindmarsh, P. Holmlund, J. W. Holt, R. W. Jacobel, A. Jenkins, W. Jokat, T. Jordan, E. C. King, J. Kohler, W. Krabill, M. Riger-Kusk, K. A. Langley, G. Leitchenkov, C. Leuschen, B. P. Luyendyk, K. Matsuoka, J. Mouginot, F. O. Nitsche, Y. Nogi, O. A. Nost, S. V. Popov, E. Rignot, D. M. Rippin, A. Rivera, J. Roberts, N. Ross, M. J. Siegert, A. M. Smith, D. Steinhage, M. Studinger, B. Sun, B. K. Tinto, B. C. Welch, D. Wilson, D. A. Young, C. Xiangbin, and A. Zirizzotti. Bedmap2: improved ice bed, surface and thickness datasets for antarctica. *The Cryosphere*, 7(1):375–393, 2013.
- [111] Anker Weidick. Satellite image atlas of glaciers of the world: Greenland. *U.S. Geological Survey Professional Paper*, page 153, 1995.

- [112] Mariana Vertenstein, Tony Craig, Adrienne Middleton, Diane Feddema, and Chris Fischer. CESM1.0.3 users guide. *NCAR Technical Notes*, 2010.
- [113] R Smith, P Jones, B Briegleb, F Bryan, G Danabasoglu, J Dennis, J Dukowicz, C Eden, B Fox-Kemper, P Gent, M Hecht, S Jayne, M Jochum, W Large, K Lindsay, M Maltrud, N Norton, S Peacock, M Vertenstein, and S Yeager. The parallel ocean program (POP) reference manual. *Ocean Component of the Community Climate System Model (CCSM) and Community Earth System Model (CESM)*, page 141, 2010.
- [114] D.M. Lawrence, R.A. Fisher, C.D. Koven, K.W. Oleson, S.C. Swenson, G. Bonan, N. Collier, B. Ghimire, L. van Kampenhout, D. Kennedy, E. Kluzek, P.J. Lawrence, F. Li, H. Li, D. Lombardozzi, W.J. Riley, W.J. Sacks, M. Shi, M. Vertenstein, W.R. Wieder, C. Xu, A.A. Ali, A.M. Badger, G. Bisht, M.A. Brunke, S.P. Burns, J. Buzan, J. Clark, A. Craig, K. Dahlin, B. Drewniak, J.B. Fisher, M. Flanner, A.M. Fox, P. Gentine, F. Hoffman, G. Keppel-Aleks, R. Knox, S. Kumar, J. Lenaerts, L.R. Leung, W.H. Lipscomb, Y. Lu, A. Pandey, J.D. Pelletier, J. Perket, J.T. Randerson, D.M. Ricciuto, B.M. Sanderson, A. Slater, Z.M. Subin, J. Tang, R. Q. Thomas, M. Val Martin, and X. Zeng. CLM5 documentation. *NCAR Technical Notes*, page 350, 2016.
- [115] Keith W Oleson, David M Lawrence, Mark G Flanner, Erik Kluzek, Samuel Levis, Sean C Swenson, E Thornton, Aiguo Dai, Mark Decker, Robert Dickinson, Johannes Feddema, Colette L Heald, Jean-Francois Lamarque, Guo-Yue Niu, Taotao Qian, Steve Running, Koichi Sakaguchi, Andrew Slater, Reto Stekli, Aihui Wang, Liang Yang, Xiaodong Zeng, and Xubin Zeng. Technical description of version 4.0 of the community land model (CLM). *NCAR Technical Notes*, page 266, 2010.
- [116] Elizabeth C Hunke and William H Lipscomb. CICE: the los alamos sea ice model documentation and software users manual version 4. page 76, 2010.
- [117] David Bailey, Cecile Hannay, Marika Holland, and Richard Neale. Slab ocean model forcing.
- [118] UCAR. Simpler models | slab ocean model.
- [119] N. Herold, R.D. Mller, and M. Seton. Comparing early to middle miocene terrestrial climate simulations with geological data. *Geosphere*, 6(6):952–961, 2010.
- [120] Michael P. Meyers, Paul J. DeMott, and William R. Cotton. New primary ice-nucleation parameterizations in an explicit cloud model. *Journal of Applied Meteorology*, 31(7):708–721, 1992.
- [121] Alexei V. Korolev and Ilia P. Mazin. Supersaturation of water vapor in clouds. *Journal of the Atmospheric Sciences*, 60(24):2957–2974, 2003.
- [122] I. Koren, L. A. Remer, O. Altaratz, J. V. Martins, and A. Davidi. Aerosol-induced changes of convective cloud anvils produce strong climate warming. *Atmospheric Chemistry and Physics*, 10(10):5001–5010, 2010.